Article

Cell Reports

KMT2B Is Selectively Required for Neuronal Transdifferentiation, and Its Loss Exposes Dystonia Candidate Genes

Graphical Abstract

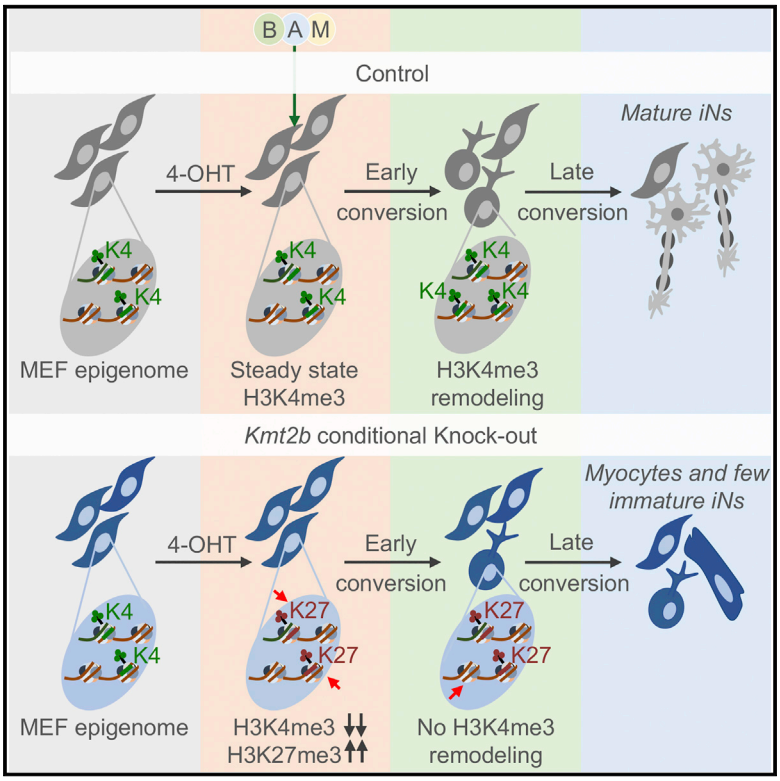

Highlights

- KMT2B is critical for neuronal transdifferentiation, whereas KMT2A is dispensable
- KMT2B is responsible for the activation of the neuronal maturation gene program
- KMT2B represses the myocyte fate unleashed upon defective transdifferentiation
- KMT2B dependence reveals candidate dystonia-causative genes

Authors

Giulia Barbagiovanni, Pierre-Luc Germain, Michael Zech, ..., Adrian Francis Stewart, Juliane Winkelmann, Giuseppe Testa

Correspondence

giuseppe.testa@ieo.it

In Brief

Barbagiovanni et al. demonstrate that KMT2B, in contrast to KMT2A, is fundamental for the epigenetic and transcriptomic resetting underlying transdifferentiation of fibroblasts into induced neuronal cells (iNs), acting both in the suppression of alternative fates and in the promotion of iN maturation. Transdifferentiation-specific KMT2B targets reveal dystonia-causative gene candidates.

Data and Software Availability

GSE120441

Barbagiovanni et al., 2018, Cell Reports *25*, 988–1001
October 23, 2018
https://doi.org/10.1016/j.celrep.2018.09.067

CellPress

OPEN ACCESS
CellPress

Cell Reports
Article

KMT2B Is Selectively Required for Neuronal Transdifferentiation, and Its Loss Exposes Dystonia Candidate Genes

Giulia Barbagiovanni,[1] Pierre-Luc Germain,[1,12] Michael Zech,[2,3] Sina Atashpaz,[1,13] Pietro Lo Riso,[1] Agnieszka D'Antonio-Chronowska,[1,14] Erika Tenderini,[1] Massimiliano Caiazzo,[4,15] Sylvia Boesch,[5] Robert Jech,[6] Bernhard Haslinger,[3] Vania Broccoli,[4,7] Adrian Francis Stewart,[8] Juliane Winkelmann,[2,9,10] and Giuseppe Testa[1,11,16,*]

[1]Department of Experimental Oncology, IEO, European Institute of Oncology IRCCS, 20139 Milan, Italy
[2]Institut für Neurogenomik, Helmholtz Zentrum München, 85764 Munich, Germany
[3]Klinik und Poliklinik für Neurologie, Klinikum rechts der Isar, Technische Universität München, 81675 Munich, Germany
[4]San Raffaele Scientific Institute, 20132 Milan, Italy
[5]Department of Neurology, Medical University Innsbruck, 6020 Innsbruck, Austria
[6]Department of Neurology and Center of Clinical Neuroscience, First Faculty of Medicine, Charles University and General Faculty Hospital, 12821 Prague, Czech Republic
[7]National Research Council (CNR), Institute of Neuroscience, 20129 Milan, Italy
[8]Genomics, Biotechnology Center, Center for Molecular and Cellular Bioengineering, Technische Universität Dresden, 01069 Dresden, Germany
[9]Lehrstuhl für Neurogenetik und Institut für Humangenetik, Technische Universität München, 81675 Munich, Germany
[10]Munich Cluster for Systems Neurology, SyNergy, 81829 Munich, Germany
[11]Department of Oncology and Hemato-Oncology, University of Milan, 20122 Milan, Italy
[12]Present address: Institute for Neurosciences, D-HEST, ETH Zürich, 8057 Zürich, Switzerland
[13]Present address: DNA Metabolism Laboratory, IFOM – The FIRC Institute of Molecular Oncology, 20139 Milan, Italy
[14]Present address: Institute for Genomic Medicine, University of California, San Diego, La Jolla, CA 92093, USA
[15]Present address: Department of Pharmaceutics, Utrecht Institute for Pharmaceutical Sciences (UIPS), Utrecht University, 3584 CG Utrecht, the Netherlands
[16]Lead Contact
*Correspondence: giuseppe.testa@ieo.it
https://doi.org/10.1016/j.celrep.2018.09.067

SUMMARY

Transdifferentiation of fibroblasts into induced neuronal cells (iNs) by the neuron-specific transcription factors *Brn2*, *Myt1l*, and *Ascl1* is a paradigmatic example of inter-lineage conversion across epigenetically distant cells. Despite tremendous progress regarding the transcriptional hierarchy underlying transdifferentiation, the enablers of the concomitant epigenome resetting remain to be elucidated. Here, we investigated the role of KMT2A and KMT2B, two histone H3 lysine 4 methylases with cardinal roles in development, through individual and combined inactivation. We found that *Kmt2b,* whose human homolog's mutations cause dystonia, is selectively required for iN conversion through suppression of the alternative myocyte program and induction of neuronal maturation genes. The identification of KMT2B-vulnerable targets allowed us, in turn, to expose, in a cohort of 225 patients, 45 unique variants in 39 KMT2B targets, which represent promising candidates to dissect the molecular bases of dystonia.

INTRODUCTION

The conversion of murine embryonic fibroblasts (MEFs) into induced neuronal cells (iNs) through forced expression of the *Brn2*, *Ascl1*, and *Myt1l* transcription factors (TFs) (hereafter called BAM [Brn2, Ascl1, Mytl1] factors) defined the paradigm of transdifferentiation across germ layers (Vierbuchen et al., 2010). BAM factors synergistically cooperate in this process (~20% efficiency), which does not require either proliferation or the transient reacquisition of pluripotency (Vierbuchen et al., 2010). ASCL1 instructs transdifferentiation as a pioneer TF, recognizing trivalent chromatin states marked by H3 lysine 4 monomethylation (H3K4me1), lysine 9 trimethylation (H3K9me3), and lysine 27 acetylation (H3K27ac) (Wapinski et al., 2013). BRN2 and MYT1L are, instead, critical for iN maturation and the suppression of alternative cell fates; upon *Ascl1*-only infection, MEFs that fail to become iNs deviate toward myocytes, an outcome that is prevented by co-transduction with *Brn2* and *Myt1l* (Mall et al., 2017; Treutlein et al., 2016; Wapinski et al., 2013).

ASCL1 has been recently shown to effect massive remodeling of chromatin accessibility and nucleosome phasing, with open chromatin loci enriched for neuronal and muscle pathway genes (Wapinski et al., 2017). Moreover, MEF-to-iN conversion features a major chromatin reconfiguration in the first 5 days after *Ascl1* induction, following which further chromatin transitions

represent less than 20% of all changes underlying direct neuronal conversion (Wapinski et al., 2017). This suggests that these epigenetic transitions are not as gradual as during reprogramming to pluripotency (Cacchiarelli et al., 2015; Chronis et al., 2017), but the role of specific chromatin regulators in these accompanying waves of chromatin resetting remains elusive.

Here, we investigated the roles of KMT2A and KMT2B in MEF-to-iN conversion in light of their critical function in lineage decisions. KMT2A and KMT2B belong to Set1-Trithorax type H3K4 methylases, specifically responsible for the deposition of histone H3 lysine 4 trimethylation (H3K4me3) at gene promoters (Denissov et al., 2014).

Both associate with MENIN, which mediates their localization at specific loci, such as *HOX* genes (Glaser et al., 2006; Hughes et al., 2004; Lee et al., 2006). Despite their high homology, KMT2A and KMT2B are spatially and temporally non-redundant. Thus, knockout (KO) of either *Kmt2a* (Ernst et al., 2004) or *Kmt2b* (Glaser et al., 2006) is embryonic lethal at embryonic day 12.5 (E12.5) or E.10.5, respectively. Furthermore, KMT2A and KMT2B have specific roles during mammalian neuronal differentiation. During retinoic acid-based differentiation, the two enzymes regulate different *HOX* genes (Denissov et al., 2014), and *Kmt2b*$^{-/-}$ embryonic stem cells (ESCs) show a severe delay in *in vitro* differentiation toward the ectodermal lineage (Lubitz et al., 2007). Adult neurogenesis and function are also specifically affected. Indeed, *Kmt2a*$^{-/-}$ subventricular zone neural stem cells (SVZ NSCs) are impaired selectively in neuronal differentiation, whereas both KMT2A and KMT2B contribute to memory formation, albeit through distinct target pathways and with no apparent effects on brain and neuronal morphology (Kerimoglu et al., 2013, 2017; Lim et al., 2009). Finally, mutations in *KMT2A* and *KMT2B* cause two distinct brain disorders: Wiedemann-Steiner syndrome, featuring intellectual disability, and a newly recognized molecular subset of early-onset generalized dystonia, respectively (Meyer et al., 2017; Strom et al., 2014; Zech et al., 2016).

RESULTS

Conditional Inactivation of *Kmt2a* and *Kmt2b* upon Transdifferentiation

To study the role of KMT2A and KMT2B during transdifferentiation, we employed conditional mouse strains carrying exon 2 of *Kmt2a* and/or *Kmt2b* flanked by LoxP sites, the knockin of the *YFP*-coding gene into one *Rosa26* allele downstream of a LoxP-flanked transcription termination cassette (STOP cassette), and the gene coding for the tamoxifen-inducible version of *Cre* recombinase knocked into the second *Rosa26* allele (Glaser et al., 2006; Kranz et al., 2010; Testa et al., 2004). Upon 4-hydroxytamoxifen (4-OHT) administration, *Cre* is expressed, generating a frameshift mutation in *Kmt2a* and/or *Kmt2b* (Figure 1A). MEFs were derived from *Kmt2a* (and/or *Kmt2b*)$^{fl/fl}$ *Cre*$^{+}$ *YFP*$^{+}$ embryos and from *Kmt2a*$^{+/+}$*Kmt2b*$^{+/+}$ *Cre*$^{+}$ *YFP*$^{+}$ or *Kmt2a*$^{fl/+}$ *Cre*$^{+}$ *YFP*$^{+}$ for *Kmt2a* conditional KO (cKO) as controls (Figure 1A). After 5 days of 4-OHT treatment followed by either 2 or 7 days in normal medium (Figure 1B), depletion of *Kmt2a* and/or *Kmt2b* was assessed by qRT-PCR (Figure 1C) and western blot (Figure 1D).

Transdifferentiation was then implemented according to the original protocol (Vierbuchen et al., 2010; Figure 1B). The sustained expression of *YFP* (Figure S1A) along with permanent loss of *Kmt2b* exon 2 (Figure S1B) through the end of transdifferentiation excluded selection of *Kmt2b*$^{fl/fl}$ iNs that might have escaped recombination.

To decipher the role of the two KMT2 methylases, we integrated two complementary approaches to capture the acquisition of iN identity along transdifferentiation: morphological analysis through an automated and unbiased imaging method (ScanR) and cytofluorimetric analysis (fluorescence-activated cell sorting [FACS]) for the expression of polysialic acid-neural cell adhesion molecule (PSA-NCAM), a marker of iN induction (Figure 1B). Transcriptomic and epigenomic profiling was then performed at 5 and 13 days of transdifferentiation (Figure 1B). Day 5 was chosen as reference starting point because, at this time, MEFs are still equally competent to become iNs, having all undergone convergent transcriptional changes (Treutlein et al., 2016). Day 13 was selected as the endpoint because 8 days following transduction no more iNs are induced, and the 13-day iNs have been shown to be functionally mature (Vierbuchen et al., 2010). MEFs were also profiled at the epigenomic level at the onset of transdifferentiation to define their initial chromatin configuration (Figure 1B).

Kmt2b Ablation Impairs Transdifferentiation

We evaluated the transdifferentiation potential of *Kmt2a*$^{-/-}$ and/or *Kmt2b*$^{-/-}$ MEFs in terms of both efficiency of iN generation and degree of their maturation. To distinguish between the effect of their loss on cell mortality and transdifferentiation, we harnessed the observation that already 1 day after doxycycline administration (day 3), the vast majority of cells are post-mitotic (Vierbuchen et al., 2010). To confidently ascribe any change in cell number to cell mortality rather than to cell proliferation, we selected cKO and control samples starting transdifferentiation from the empirically validated same number of cells on day 3.

We found that loss of *Kmt2b* greatly impaired transdifferentiation efficiency in a manner independent of the mortality rate that accompanies transdifferentiation (Figures 2A and 2B; Table S1). In contrast, for the loss of *Kmt2a*, transdifferentiation efficiency was correlated with cell viability (Figures S1C and S1D; Table S1), pointing to the former as a by-product of the latter.

Next we sought to determine whether there is any redundancy between the two methylases by knocking out both enzymes. *Kmt2a*$^{-/-}$*Kmt2b*$^{-/-}$ transdifferentiated MEFs showed both the highest cell death and the lowest conversion efficiency, indicating that KMT2A only partially compensates for the lack of KMT2B during transdifferentiation (Figures 2A and 2B; Table S1). Importantly, the combined loss of *Kmt2a* and *Kmt2b* did not affect MEF viability per se but was specifically triggered upon induction of transdifferentiation (Figures S1E and S1F).

We confirmed these observations through FACS-based quantitation of PSA-NCAM^{+} cells. Indeed, both *Kmt2a*$^{-/-}$ and *Kmt2b*$^{-/-}$ MEFs showed a lower efficiency of iN induction with respect to controls (Figure 2C), but although, for *Kmt2a*$^{-/-}$ MEFs, this was entirely accounted for by the higher rate of cell death (Figures 2D, S1G and S1H), for *Kmt2b*$^{-/-}$ MEFs, it was independent of cell death and, thus, imputable to a specific

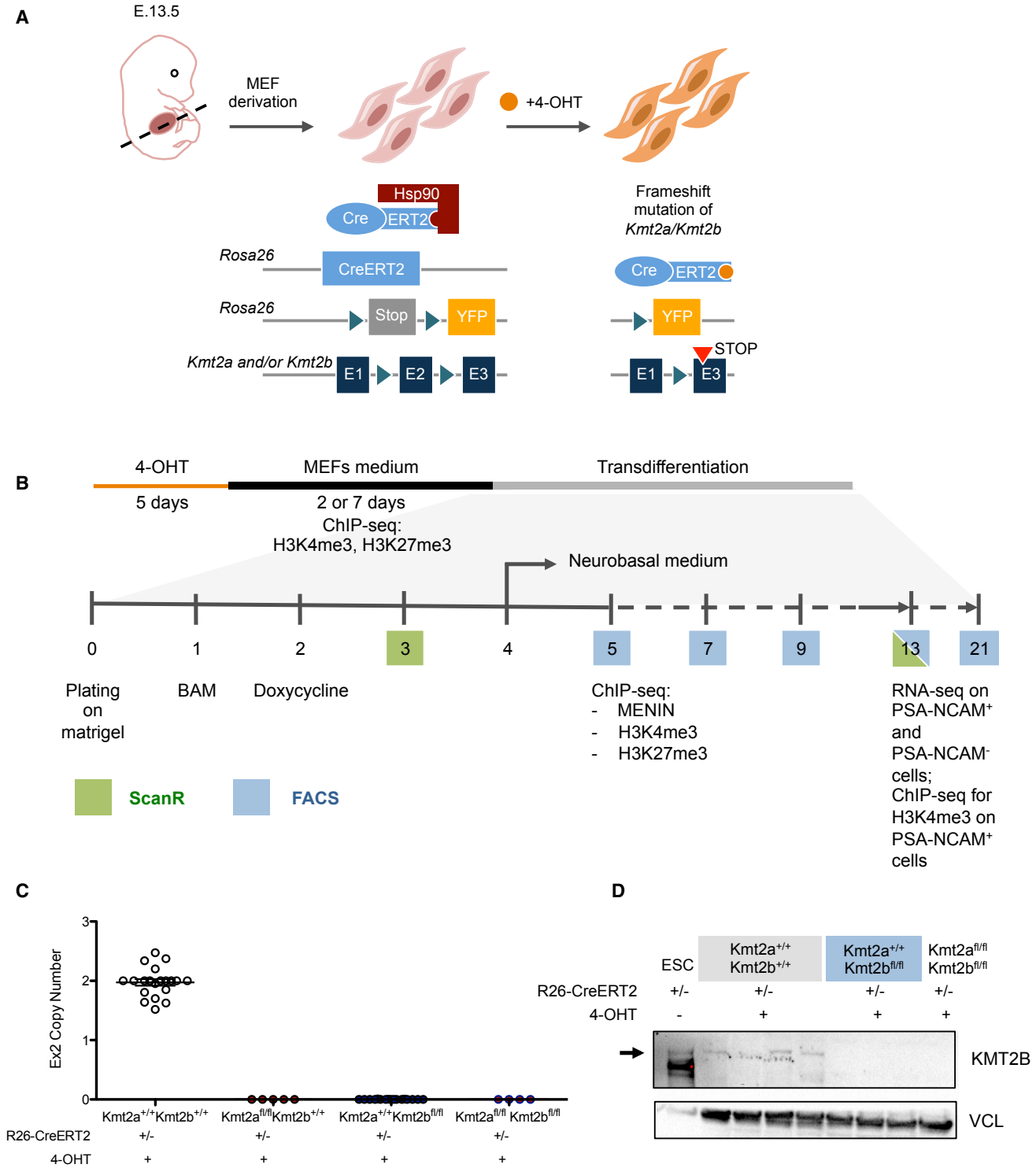

Figure 1. Experimental System

(A) Schematic of *Kmt2* cKO MEF derivation and 4-OHT treatment.

(B) Schematic of our experimental pipeline.

(C) Representative qPCR results for exon 2 copy number after 4-OHT treatment. Means ± SEM.

(D) Western blot analysis for KMT2B, with VINCULIN (VCL) as housekeeping, of MEFs treated 5 days with 4-OHT and left 7 days in culture without 4-OHT. The first lane was dedicated to ESCs.

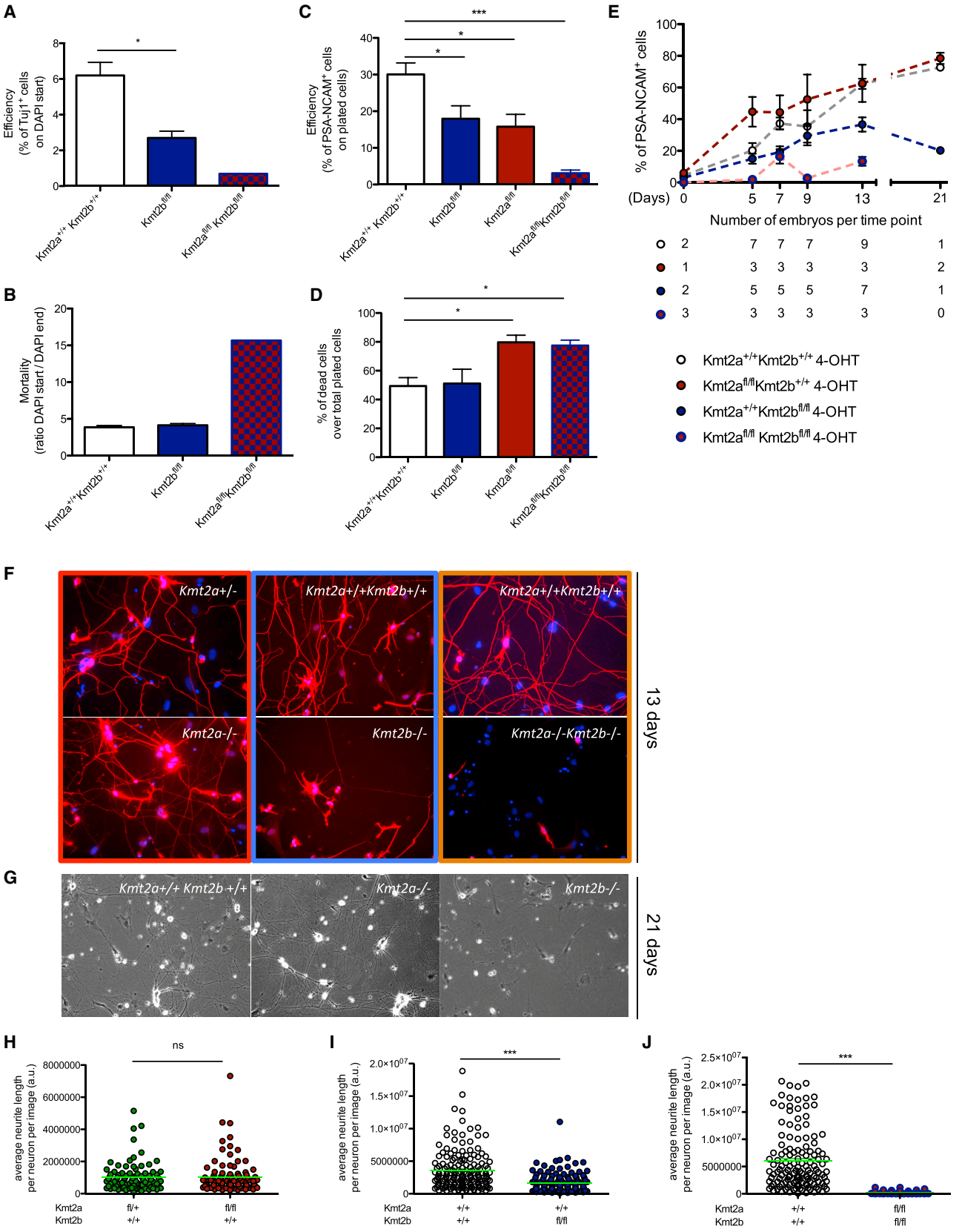

(legend on next page)

requirement for KMT2B in transdifferentiation (Figures 2D, S1I and S1J). Moreover, although cell mortality in *Kmt2a*$^{-/-}$ transdifferentiating MEFs was higher with respect to *Kmt2b*$^{-/-}$ and controls (Figure 2D), the percentage of *Kmt2a*$^{-/-}$ PSA-NCAM^{+} cells overlapped or was even higher than in controls along the entire process (Figure 2E). This indicates that PSA-NCAM^{+} and PSA-NCAM^{-} fractions are at least equally vulnerable to cell death across *Kmt2a*$^{-/-}$ and *Kmt2a*$^{+/+}$.

Finally, FACS analysis of the combined KO showed that, although the viability of *Kmt2a*$^{-/-}$*Kmt2b*$^{-/-}$ MEFs was comparable with that of *Kmt2a*$^{-/-}$ and lower than that of controls (Figures 2D, S1K and S1L), their transdifferentiation efficiency was strongly reduced with respect both to control and the single cKO transdifferentiating MEFs (Figure 2C), underscoring that KMT2B is the main H3K4 trimethylase involved in direct cell conversion.

Then we analyzed the morphology of the generated iNs to probe the role of either methylase on iN maturation. To this aim, we investigated neurite elongation as a defining hallmark of complete iN conversion, finding that, in *Kmt2b*$^{-/-}$ iNs, it was severely reduced both at 13 (Figures 2F, 2I, S2A, and S2B) and 21 days (Figure 2G) of transdifferentiation. On the contrary, and consistent with the unaltered efficiency of iN conversion, neurite length in *Kmt2a*$^{-/-}$ iNs was fully comparable with that of *Kmt2a*$^{+/-}$ (Figures 2F, 2G, 2H, S2C, and S2D). Finally, the few double cKO iNs only showed minimal neurite elongation (Figures 2F, 2J, and S2E). This demonstrates that KMT2B, besides playing a fundamental role in MEF-to-iN conversion, has also a specific effect on iN maturation.

KMT2B Controls Transcriptome Resetting in MEF-to-iN Conversion

Given the role of KMT2B in H3K4me3 deposition at promoters (Denissov et al., 2014), its loss could impair the gene expression program underlying MEF-to-iN transition. To unveil the molecular basis of the dual phenotype observed upon loss of KMT2B (namely, less efficient iN conversion and defective iN maturation), we performed RNA sequencing (RNA-seq) on sorted PSA-NCAM^{+} and PSA-NCAM^{-} *Kmt2b*$^{-/-}$ and control cells at day 13 of transdifferentiation. In particular, through the analysis of PSA-NCAM^{+} transcriptomes, we aimed to establish which genes responsible for transdifferentiation were differentially expressed in the absence of KMT2B and how *Kmt2b*$^{-/-}$ iNs differed from controls. Instead, through PSA-NCAM^{-} transcriptomic profiling, we pursued mechanistic insight into the effect of *Kmt2b* loss on MEF-to-iN conversion.

The first component identified by principal-component analysis (PCA) clearly distinguished genotypes in both PSA-NCAM populations (Figures S3A and S3B), indicating that *Kmt2b* status represents the largest source of variation in the datasets. Specifically, through the analysis of PSA-NCAM^{+} cells, we found 1,508 differentially expressed genes (DEGs) between *Kmt2b*$^{-/-}$ and control iNs (at false discovery rate [FDR] < 0.01 and with at least a 50% fold change), the majority of which were downregulated in the latter, consistent with the gene-activating function of KMT2B (Figure 3A). To define which stage of transdifferentiation was most affected by loss of KMT2B, we clustered day 13 DEGs between *Kmt2b*$^{-/-}$ and control iNs using K-means clustering according to their established expression pattern throughout transdifferentiation (Wapinski et al., 2013; Figure 3B). Genes that are normally expressed on day 15 and downregulated on day 24 of transdifferentiation (clusters 2 and 3) were found to be already lowly expressed at 13 days in our *Kmt2b*$^{-/-}$ samples, further highlighting a defective MEF-to-iN transition. On the other hand, a high proportion of cluster 4, whose expression gradually increases throughout transdifferentiation, peaking at day 24, and that is enriched for synaptic genes and RE1-silencing transcription factor (REST) targets (4.79-fold enrichment, q-value [q] $\sim$ 1e−54 in neuronal progenitors), was downregulated in *Kmt2b*$^{-/-}$ iNs, further corroborating the defective neuronal fate acquisition in the absence of KMT2B.

Recently, Treutlein et al. (2016) integrated the single-cell transcriptomes of *Ascl1*-only infected MEFs throughout transdifferentiation with those of 15-day BAM-infected iNs and identified the transcriptional regulators that most likely coordinate transdifferentiation progression, defining three subnetworks (i.e., MEF, initiation and maturation). We found that, in our PSA-NCAM^{+} dataset, the most disrupted subnetwork by loss of KMT2B was the maturation one, confirming at the molecular level the defective iN maturation phenotype we observed (Figure 3C). Indeed, the top 30 DEGs (Figures 3A and S3C) that have annotated function(s) included four key promoters of physiological neurite

Figure 2. KMT2B Is Essential for MEF-to-iN Transition

(A) Efficiency of transdifferentiation in ScanR experiments, calculated relating, for any chosen concentration, the number of Tuj1^{+} at 13 days to the number of DAPI 3 days after plating.

(B) Cell mortality in ScanR experiments, calculated as the ratio of DAPI 3 days (DAPI start) and 13 days (DAPI end) after plating.

(A and B) *Kmt2a*$^{+/+}$*Kmt2b*$^{+/+}$, n = 3; *Kmt2b*$^{fl/fl}$, n = 2; *Kmt2a*$^{fl/fl}$*Kmt2b*$^{fl/fl}$, n = 1.

(C) Efficiency of transdifferentiation in FACS experiments, calculated relating the number of PSA-NCAM^{+} cells at 13 days to the number of plated cells.

(D) Percentage of dead cells, calculated at 13 days, over the initial number of plated MEFs.

(C and D) The number of independent embryos per genotype corresponds to the one reported for time point 13 days of (E).

(E) Percentage of PSA-NCAM^{+} cells among transdifferentiating MEFs 5, 7, 9, 13, and 21 days after plating, assayed with FACS analysis. The number of independent embryos per time point per genotype is reported under the graph.

(F) Representative images of three different experiments, each reporting the specific cKO and its control. *Kmt2a*$^{fl/-}$ (top left), *Kmt2a*$^{+/+}$*Kmt2b*$^{+/+}$ (top, center and right), *Kmt2a*$^{-/-}$ (bottom left), *Kmt2b*$^{-/-}$ (bottom center), and *Kmt2a*$^{-/-}$*Kmt2b*$^{-/-}$ (bottom right) iNs at 13 days are reported (DAPI in blue and Tuj1 in red).

(G) Representative images of 21-day *Kmt2a*$^{+/+}$*Kmt2b*$^{+/+}$ (left), *Kmt2a*$^{-/-}$ (center), and *Kmt2b*$^{-/-}$ (right) iNs acquired with the bright-field microscope.

(H–J) Average neurite length per neuron, calculated with Neuritetracer on day 13 of transdifferentiation. In particular Kmt2a$^{-/-}$ iNs (H), Kmt2b$^{-/-}$ iNs (I), and Kmt2a$^{-/-}$ Kmt2b$^{-/-}$ iNs (J) were compared to controls.

In the case of *Kmt2a* ScanR experiments (F and H), *Kmt2a*$^{fl/-}$ MEFs were used as a control. In (F), (H), and (J), MEFs were plated for BAM transduction 2 days after 4-OHT, whereas, in (A)–(E), (G), and (I), MEFs were plated 7 days after 4-OHT. (A)–(E) and (H)–(J), means ± SEM; ***p < 0.0001; *p < 0.01; ns, not significant.

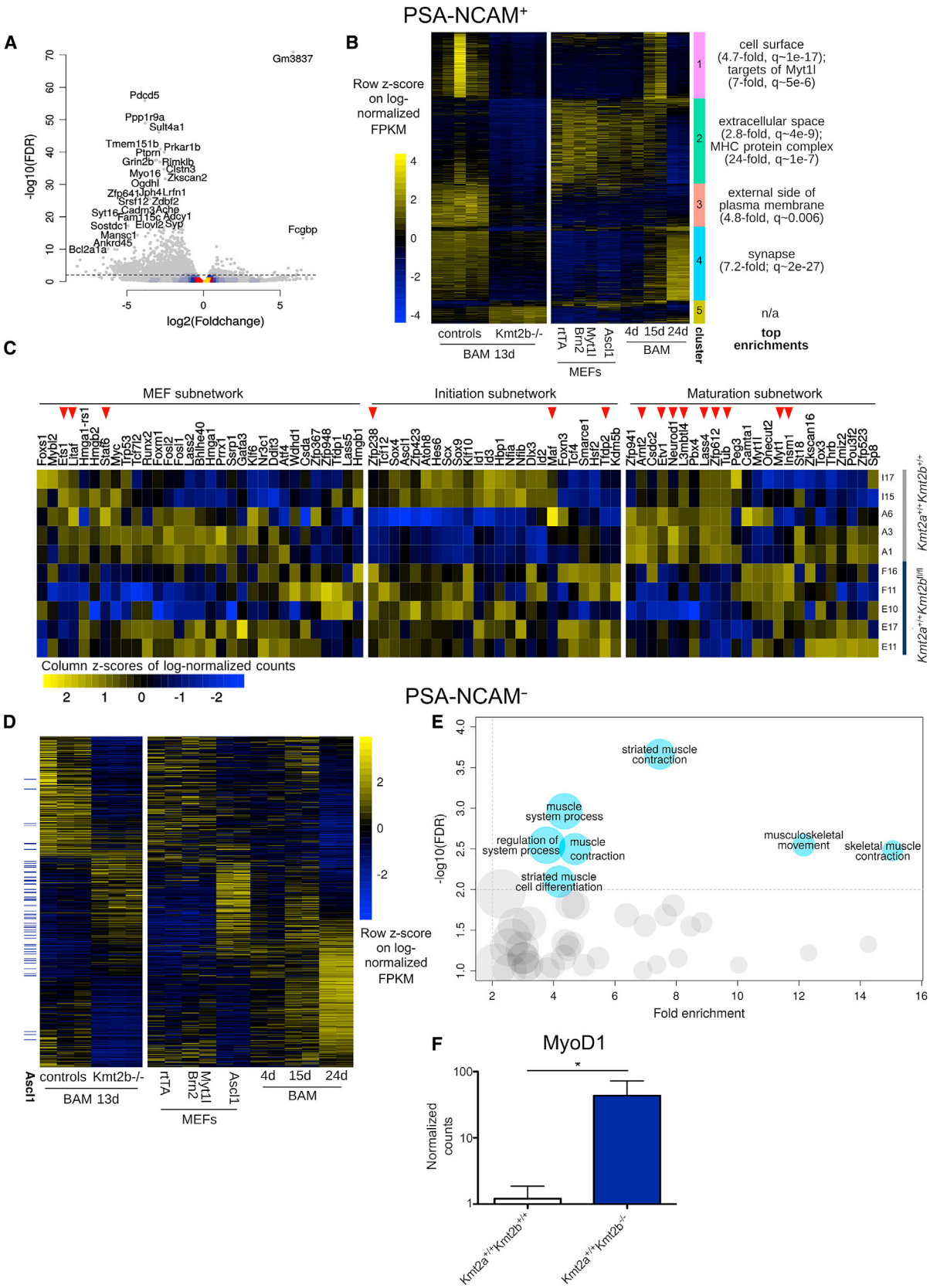

(legend on next page)

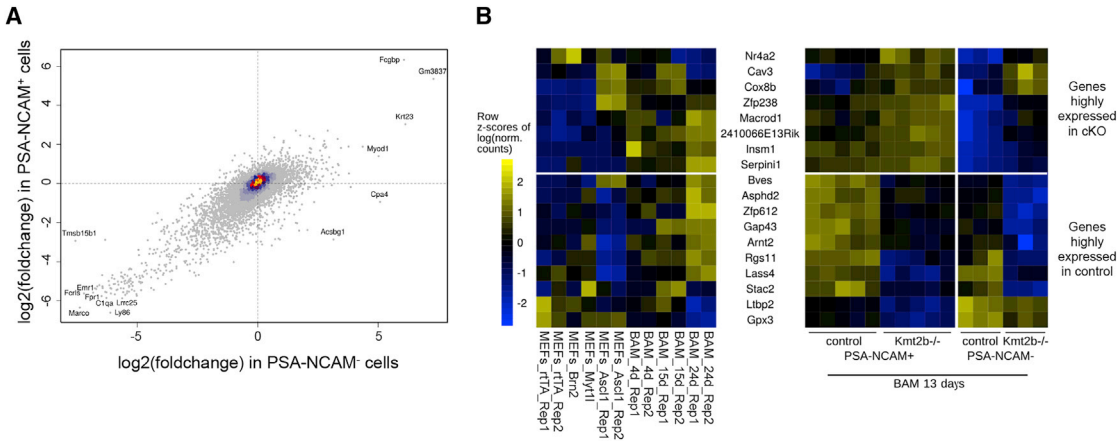

Figure 4. Early Dysregulation of MEF-to-iN Conversion in the Absence of KMT2B

(A) Correlation of fold changes in *Kmt2b*$^{-/-}$ across PSA-NCAM^{-} and PSA-NCAM^{+} cells. All tested genes are plotted.

(B) Heatmap of expression across normal transdifferentiation (left) and on day 13 (right) of DEGs with genome-wide significance in both cell fractions and also significantly differentially expressed during normal transdifferentiation. *Z* scores were calculated separately for the left and right portions of the heatmap.

extension *(Ppp1r9a*, *Myo16*, *Lrfn1*, and *Prka1b)* and nine regulators of synapse formation, maturation, and function (*Clstn3*, *Jph4*, *Syp, Sult4a1*, *Ptprn*, *Cadm3*, *Adcy1*, *Grin2b*, and *Ache*). Together, these results show that the defective iN phenotype observed upon loss of KMT2B is determined by dysregulation of the transcriptional program sustaining iN maturation.

To gain deeper insight into this phenomenon, we next compared the transcriptomes of our 13-day iNs with those of single cells undergoing MEF-to-iN transition (Treutlein et al., 2016). Strikingly, *Kmt2b*$^{-/-}$ PSA-NCAM^{+} iNs showed a higher correlation with the transcriptomes of earlier stages of transdifferentiation, providing the molecular basis for our observation that the few *Kmt2b*$^{-/-}$ MEFs that manage to convert to iNs fail to undergo complete neuronal maturation (Figures S3D and S3E). Furthermore, these maturation-defective iNs also present an increased correlation with myocyte gene expression, suggesting a concomitant failure to fully suppress alternative fates (Figures S3D and S3E). Thus, to confirm whether *Kmt2b*$^{-/-}$ MEFs, which transdifferentiated less efficiently than controls, switched toward the myocyte fate, we compared *Kmt2b*$^{-/-}$ and control PSA-NCAM^{-} 13-day transcriptomes and found that upregulated genes in *Kmt2b*$^{-/-}$ PSA-NCAM^{-} cells were significantly enriched for targets bound by ASCL1 in the first phases of transdifferentiation (Wapinski et al., 2013; Figure 3D). Although these ASCL1-bound genes have been identified in MEFs transduced either with this TF alone (3.9-fold, p ~ 2e−7) or with all BAM factors (3-fold, p ~ 2e−10), a large fraction is then rapidly repressed by BRN2 and MYT1L in BAM-transduced MEFs (Figure 3D), preventing the shift toward myocytes (Treutlein et al., 2016). Therefore, the enrichment for such genes in *Kmt2b*$^{-/-}$ PSA-NCAM^{-} cells indicates that loss of KMT2B prevents their expected silencing, rerouting conversion toward alternative fates.

Consistent with this observation, the top gene ontology (GO) enrichments of upregulated genes in *Kmt2b*$^{-/-}$ PSA-NCAM^{-} cells were all related to myocyte fate acquisition and function (Figure 3E). Moreover, among these genes, we scored a 35-fold increase in *MyoD1*, a fundamental driver of myogenic differentiation (Pinney et al., 1988; Figure 3F).

Because we observed a very high correlation in fold changes between the transcriptomes (correlation [cor] ~ 0.8, p ~ 2e−16) of PSA-NCAM^{+} and PSA-NCAM^{-} fractions (Figure 4A), we hypothesized that much of the impairment in *Kmt2b*$^{-/-}$ transcriptomic resetting occurred early during MEF-to-iN transition. Thus, we analyzed the genes that changed in the same direction in both PSA-NCAM fractions and whose level of expression is regulated during transdifferentiation (Wapinski et al., 2013). Indeed, most of the genes downregulated in the absence of KMT2B in both fractions are upregulated in the first phases of transdifferentiation (Figure 4B), and among them, we found the genes of the maturation subnetwork, *Zfp612*, *Arnt2,* and *Lass4*. In particular, *Arnt2* and *Zfp612* are upregulated or remain expressed only when MEFs are transduced with either *Brn2* or *Myt1l* or all BAM factors but not with *Ascl1* alone. Hence, in the absence of KMT2B, these

Figure 3. KMT2B Loss Impairs Transcriptomic Changes Underlying Transdifferentiation

(A) Volcano plot highlighting the top DEGs among *Kmt2b*$^{-/-}$ and control 13-day iNs.

(B) DEGs upon *Kmt2b* KO clustered on the basis of their expression pattern across stages of transdifferentiation (plotted are log-normalized fragments per kilobase pair per million reads sequenced [FPKM], scaled across the whole dataset).

(C) Heatmap showing the expression across genotypes in iNs sorted at 13 days of the transcriptional regulators belonging to the three subnetworks described by Treutlein et al. (2016). The significant DEGs between *Kmt2b*$^{-/-}$ and the control are indicated by red arrows. Each line represents a different embryo from which the MEFs were derived.

(D) Expression pattern during normal transdifferentiation (right) and across genotypes on day 13 (left) of the DEGs found in 13-day *Kmt2b*$^{-/-}$ PSA-NCAM^{-} cells.

(E) GO enrichment analysis of genes upregulated in 13-day *Kmt2b*$^{-/-}$ PSA-NCAM^{-} cells with respect to controls.

(F) *MyoD1* normalized counts in control and *Kmt2b*$^{-/-}$ PSA-NCAM^{-} cells. Means ± SD are reported. *, FDR < 0.01.

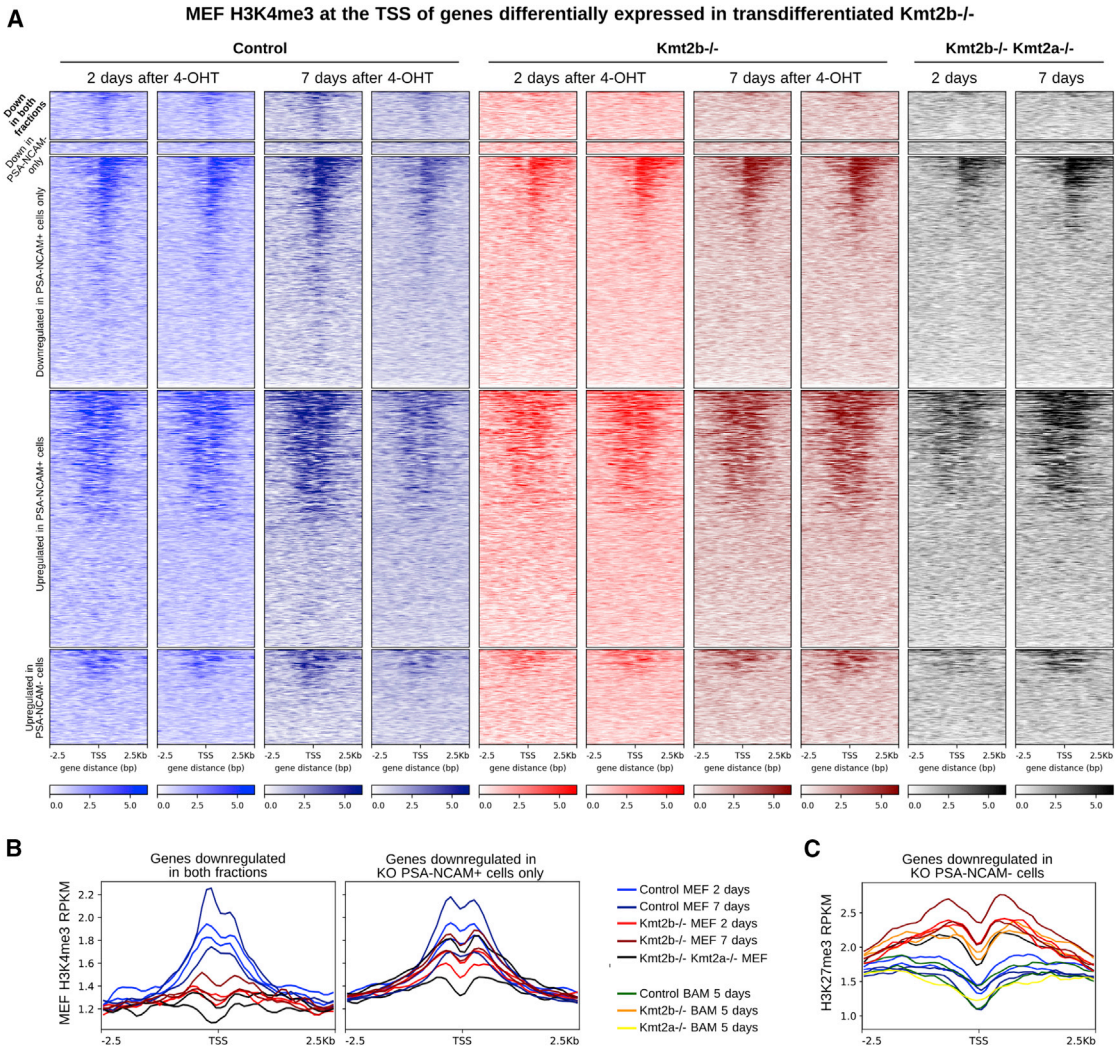

Figure 5. The Histone Methylation Patterns of *Kmt2b*$^{-/-}$ MEFs Prefigure Gene Repression in Untransdifferentiated cKO Cells

(A) MEF H3K4me3 coverage (in reads per kilobase million [RPKM]) in *Kmt2b*$^{-/-}$, control, and double-mutant MEFs 2 and 7 days after the last 4-OHT administration around the TSS of DEGs in *Kmt2b*$^{-/-}$ and control transdifferentiating cells.

(B) MEF H3K4me3 RPKM around the TSS of genes downregulated in both PSA-NCAM fractions (left) and in *Kmt2b*$^{-/-}$ PSA-NCAM^{+} cells only (right).

(C) H3K27me3 RPKM around the TSS of genes downregulated in *Kmt2b*$^{-/-}$ PSA-NCAM^{-} cells, in MEFs, and at 5 days of transdifferentiation.

genes could not be activated despite the presence of *Brn2* and *Myt1l*. Furthermore, one of the main direct targets of ASCL1, the repressor ZFP238 (Wapinski et al., 2013), was deregulated both in PSA-NCAM^{+} and PSA-NCAM^{-} *Kmt2b*$^{-/-}$ fractions with respect to controls (Figure 4B), underscoring that the loss of KMT2B disrupts the dynamic interplay among BAM factors on their targets.

Together, the combined transcriptomic analysis of PSA-NCAM^{+} and PSA-NCAM^{-} cKO and control cells demonstrates that, upon transdifferentiation, *Kmt2b*$^{-/-}$ MEFs undergo an early massive dysregulation of the transcriptional program enabling conversion. This, on one side, leads to a lower transdifferentiation efficiency and a substantial shift toward a myocytic fate; on the other, it prevents the few converting *Kmt2b*$^{-/-}$ cells from activating the full neuronal maturation program.

Elucidation of the KMT2B-Vulnerable Epigenome

Next, we proceeded to analyze how the epigenome resetting underlies MEF-to-iN conversion. To define how KMT2B loss affects the balance between H3K4me3 and histone H3 lysine 27 trimethylation (H3K27me3) deposition at specific loci (Austenaa et al., 2012), we performed chromatin immunoprecipitation coupled to deep sequencing (ChIP-seq) on MEFs 2 and 7 days after 4-OHT administration. We first observed that most of the genes that were downregulated in both cell fractions (i.e., PSA-NCAM^{+} and PSA-NCAM^{-}) were H3K4me3-marked in control MEFs and lost this mark already 2 days after 4-OHT administration in *Kmt2b*$^{-/-}$ MEFs (Figure 5A). The loss of KMT2B had, instead, a milder effect, and on a smaller proportion of the transcription start site (TSS), for the genes downregulated in PSA-NCAM^{+} cells (Figures 5A and 5B). Moreover, the decrease

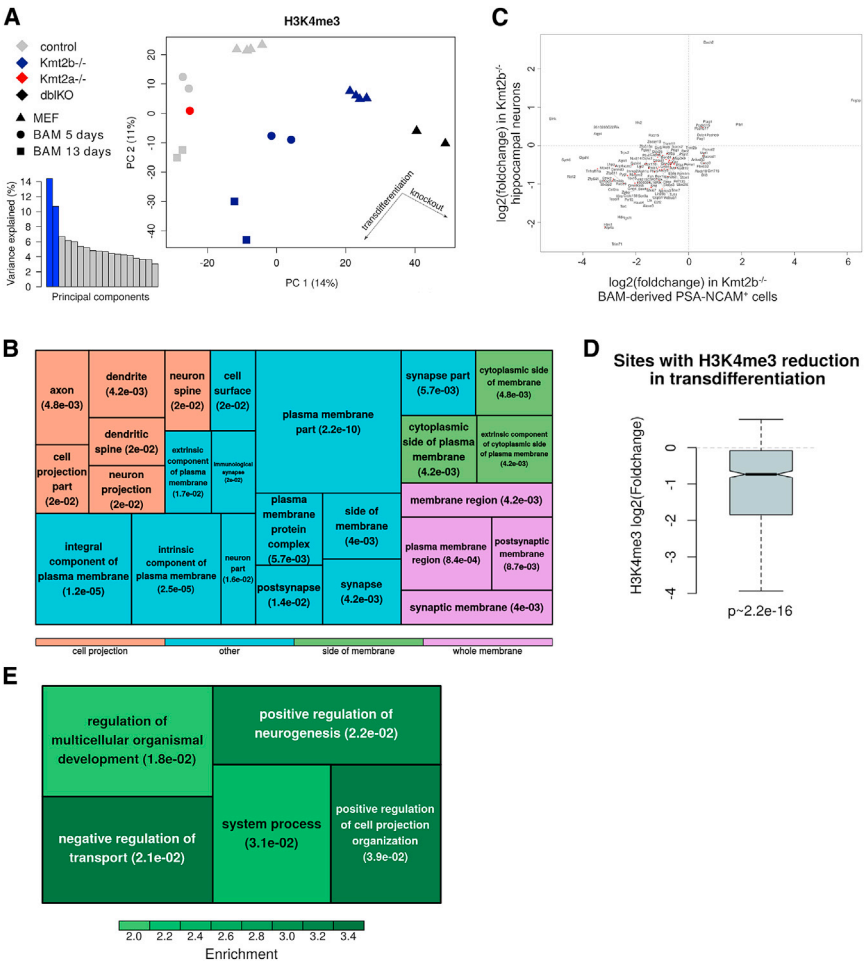

Figure 6. H3K4me3 Remodeling along Neuronal Transdifferentiation and Differentiation

(A) PCA across the union of H3K4me3 sites in *Kmt2b*$^{-/-}$ and control transdifferentiating MEFs at 5 and 13 days (in the latter after sorting for PSA-NCAM) and in MEFs prior to transdifferentiation.

(B) Quilt of the GO enrichment analysis regarding the cellular components of the genes both differentially H3K4 trimethylated and expressed (FDR < 0.01, fold change [FC] > 0.5) in *Kmt2b*$^{-/-}$ with respect to the control.

(C) Correlation of fold change in 13-day *Kmt2b*$^{-/-}$ iNs with fold change in *Kmt2b*$^{-/-}$ hippocampal neurons. Only genes significantly dysregulated in both datasets are plotted.

(D) Distribution of fold changes in H3K4me3 in *in vivo Kmt2b*$^{-/-}$ hippocampal neurons (Kerimoglu et al., 2017) of sites that lose H3K4me3 in transdifferentiating *Kmt2b*$^{-/-}$ versus control cells.

(E) Enrichments for biological processes among genes with decereased H3K4me3 in BAM-treated KO cells but not in CaMKII neurons, against the background of all H3K4me3-marked genes.

in H3K4me3 was accompanied by an increase in H3K27me3 at these TSS, which, already in cKO MEFs before the onset of iN conversion, had a magnitude comparable with the increase observed at 5 days of transdifferentiation (Figure 5C). This suggests that the epigenome remodeling, which rapidly follows the loss of KMT2B, disfavors MEF-to-iN conversion and, more specifically, that the initial failure of *Kmt2b*$^{-/-}$ MEFs in keeping active a specific subset of genes (Figure 5C) has a major, very early effect on transdifferentiation efficiency, whereas the effect of *Kmt2b* loss on neuronal maturation likely occurs at later steps.

Thus, to specifically dissect the epigenome resetting underlying iN maturation, we performed ChIP-seq on control and *Kmt2b*$^{-/-}$ MEFs on days 5 and 13 of transdifferentiation, also including the day 5 *Kmt2a*$^{-/-}$ background.

The *Kmt2a*$^{-/-}$ sample clustered together with controls in the PCA, further demonstrating the lack of effect of the absence of KMT2A on transdifferentiation (Figure 6A).

As expected by the ChIP-seq on MEFs, for the largest majority of differentially marked regions, the loss of H3K4me3 was maintained from day 5 to day 13, whereas, for a small subset of loci, the loss was reverted on day 13 (Figure S4A). The latter were particularly enriched for genes related to the regulation of nervous system development (2.4-fold enrichment, q ~ 0.009) and intracellular ligand-gated ion channel activity (15-fold enrichment, q ~ 0.007), suggesting delayed compensation on a subset of KMT2B targets enabling the acquisition, albeit severely compromised, of neuronal identity.

On the other hand, we identified 112 genes that presented lower H3K4me3 in *Kmt2b*$^{-/-}$ transdifferentiating MEFs already on day 5 and that showed a further decrease in the H3K4me3 level at 13 days. Among these, 47 were also downregulated in 13-day iNs (Figure S4B), indicating that KMT2B is necessary for the maintenance of the mark at these loci and for their sustained activation.

In light of the parallel changes in H3K4me3 on day 5 and 13 revealed by the PCA, we analyzed all samples together, adjusting for the differences linked to time points. Upon loss of *Kmt2b*, we found 994 sites, mapping at the TSS of 545 genes, showing decreased H3K4me3 and 95 sites, mapping at the TSS of 82 genes, presenting an increased H3K4me3. Among the 82 genes, only *Runx1t1* was differentially expressed in *Kmt2b*$^{-/-}$ iNs with respect to controls (Figure S4C).

We found that, of the 545 genes showing a reduced H3K4me3, 143 were significantly differentially expressed, underscoring the critical importance of KMT2B-mediated H3K4me3 deposition as a source of differential expression (overlap, p ~ 2e−59, hypergeometric test) while extending the observation that only subsets of KMT2B-dependent H3K4me3 targets are transcriptionally vulnerable (Hu et al., 2017). Some of the most significantly enriched GO categories among these genes were related to neuronal cell components (e.g., axon),

pointing to a KMT2B-mediated gene expression program whose disruption underlies defective iN specification and maturation (Figure 6B).

Next, to investigate how the role of KMT2B in transdifferentiation relates to the physiological maintenance of the neuronal fate, we compared the transcriptomic and epigenomic data of *Kmt2b*$^{-/-}$ iNs with those of *in vivo* post-mitotic hippocampal neurons (transcriptomes from whole hippocampi and H3K4me3 profiles from hippocampal neurons, respectively), in which *Kmt2b* loss was driven by Ca2+/calmodulin-dependent protein kinase II (CaMKII)-dependent *Cre* expression (Kerimoglu et al., 2017). We observed that the 116 DEGs shared between the two datasets were dysregulated in the same direction (cor p ~ 9e−7) (Figure 6C). Indeed, of the sites that lost H3K4me3 in our BAM-treated cKO cells, about 90% were detectable in some of the *in vivo* samples, and of these, 80% also showed a reduction in H3K4me3 in *Kmt2b*$^{-/-}$ hippocampal neurons (Figure 6D). Thus, loss of *Kmt2b* affects a core set of sites that lose H3K4me3 independently of the stage of neuronal determination, pointing to a fundamental convergence between the processes of iN conversion and the maintenance of physiologically acquired neuronal fate. Instead, the genes that lost the mark only in the transdifferentiation paradigm presented an enrichment for positive regulation of both neurogenesis and cell projection organization, concordant with the specific features of our impaired conversion process (Figure 6E).

Finally, to discriminate between the direct versus indirect KMT2B targets underlying the impaired transcriptomic remodeling of *Kmt2b*$^{-/-}$ MEF-to-iN transition, we set out to profile its genome-wide occupancy. To circumvent the lack of ChIP-grade commercial antibodies against KMT2B, we immunoprecipitated MENIN, the common subunit exclusive to KMT2A and KMT2B complexes, in both *Kmt2a*$^{+/+}$*Kmt2b*$^{+/+}$ and *Kmt2b*$^{-/-}$ transdifferentiating MEFs on day 5. We could thus ascribe MENIN targets in control samples to both methylases, whereas we defined by subtraction, as KMT2B-specific targets, the genes that lost MENIN binding in *Kmt2b*$^{-/-}$ with respect to control cells.

Although the low enrichment of the immunoprecipitation (IP) could only afford limited sensitivity, we could nevertheless identify candidate regions with reduced MENIN enrichment, which we intersected with promoters of genes downregulated and losing H3K4me3 in *Kmt2b*$^{-/-}$ iNs with respect to controls. This revealed a core of 12 candidate direct KMT2B target genes during iN transition (Figure S5). Importantly, these candidate direct targets included, again, *Arnt2*, a central gene of the maturation subnetwork (Treutlein et al., 2016) that, together with *Gnao1*, *Chst10*, *Rtn1*, and *Gpr135*, is related to neuronal specification, function, and metabolism.

Kmt2b Vulnerability Uncovers Candidate Genes Associated with Dystonia

It was recently shown that *KMT2B* mutations can cause early-onset dystonia (Meyer et al., 2017; Zech et al., 2016), a neurological disorder whose additional genetic causes remain still largely unknown. Indeed, the DEGs in our *Kmt2b*$^{-/-}$ samples were enriched for genes whose disruption in the mouse is associated with dystonia (*Atp1a3*, *Tubb4a*, *Hpca*, and *Gnal*) or myoclonus (*Npas4*, *Scn8a*, *Nhlrc1*, *Cit*, *Kcnj11*, *Slc7a10*, *Bsn*, *Mfsd8*, *Kcna1*, and *Plaur*) (5.7-fold, p ~ 0.0027). Thus, we exploited the 216 candidate direct KMT2B targets predicted by the intersection of DEGs (at FDR < 0.05) and genes that show H3K4me3 reduction in *Kmt2b*$^{-/-}$ over controls. In particular, we combined these targets with an analysis of genetic variations detected through high-throughput sequencing of whole exome-captured DNA from 225 dystonia patients to define candidate dystonia-relevant gene variants.

First, the analysis of the exome aggregation consortium (ExAC) population data revealed that 45 of 216 targets (21%) exhibited probability of being loss-of-function-intolerant (pLI) scores of 0.9 or higher, 54 (25%) missense *Z* scores of 2.0 or higher, and 26 (12%) both pLI scores of 0.9 or higher and missense *Z* scores of 2.0 or higher (Lek et al., 2016; Table S2). Within all targets, 34% of KMT2B target genes were evolutionary constrained against at least one class of functional variation in ExAC (Lek et al., 2016), indicating that the KMT2B-sensitive gene set is enriched for a genomic sequence in which mutational changes are scarcely tolerated. For most of the KMT2B targets (79%), we found no known disease annotation (monogenic disease) in the OMIM database (Table S2).

Under an autosomal dominant disease model, whole-exome sequencing (WES) yielded 38 unique, predicted deleterious missense variant across 32 KMT2B targets, 1 each in 38 independent probands. Of these variants, 11 affected genes with a selective constraint against missense variation (missense *Z* scores ≥ 2.0). Six genes contained heterozygous missense variants in more than 1 proband (*ALK*, *DOCK10*, *KDR*, *LRP2*, *SLC35F1*, and *SLC40A1*). In addition, a total of 7 unique predicted loss-of-function variants affecting 7 KMT2B targets were identified among 7 separate probands. Of these variants, 1 resided in a gene with strong loss-of-function intolerance in the general population (*NOL4*, pLI score of 1.0). Four variants in 3 genes emerged as especially promising candidates for follow-up evaluation (Table 1). In a female proband with childhood-onset segmental isolated dystonia and a family history suggestive of dominant inheritance (case_224), we detected a c.457C > T (p.Arg153X) stop-gain variant in the *NOL4* gene whose haploinsufficiency is predicted to be non-tolerable (pLI score of 1.0) (Lek et al., 2016); two male probands with a strikingly similar presentation of early adulthood-onset tremulous cervical isolated dystonia were each identified to have a distinct missense variant of the exact same codon 51 in *SLC35F1* (case_112: c.152G > T [p.Arg51Met]; case_122: c.152G > C [p.Arg51Thr]), a gene constrained against missense variants (missense *Z* scores of 2.01) (Figure S6B); and a female proband manifesting late adulthood-onset cervical isolated dystonia (case_088) was found to harbor a missense variant at *SLC40A1* codon 157 (c.469G > C [p.Asp157His]) (Figure S6C). Along with the observation that other missense mutations at this site have been implicated in hemochromatosis type 4 (MIM606069) (Callebaut et al., 2014; Hetet et al., 2003), a multisystem iron deposition disorder, this finding led us to reverse-phenotype this proband and uncover elevated serum ferritin levels as well as bilateral signal alterations on brain MRI in a pattern consistent with brain iron deposition (data not shown). Finally, to complete a comprehensive assessment of the mutational architecture in *KMT2B* targets among dystonia cases,

Table 1. Candidate variants in 4 probands with dystonia

Disease model	Gene	pLI score (ExAC)	missense Z score (ExAC)	Known disease annotation (OMIM)	Variation nucleotide[a]	Variation amino acid[a]	Variant type	Frequency ExAC; dbSNP142	Frequency in-house exomes[b]	CADD score	Carrier #	Sex	Age at onset, y	Dystonia type	Family history	Comment on putative disease relevance
Autosomal-dominant	*NOL4*	1.0	2.7	no	c.457C>T	p.Arg153X	stop-gain	not found; not found	not found	37	case_224	F	4	segmental isolated dystonia (cervical dystonia, upper limb dystonic tremor)	positive	loss-of-function variant in gene with pLI ≥ 0.9
Autosomal-dominant	*SLC35F1*	0.39	2.01	no	c.152G>T	p.Arg51Met	missense	not found; not found	not found	30	case_112	M	26	focal isolated dystonia (tremulous cervical dystonia)	negative	mutational recurrence at codon-51 in gene with missense Z score ≥ 2.0
Autosomal-dominant	*SLC35F1*	0.39	2.01	no	c.152G>C	p.Arg51Thr	missense	not found; not found	not found	24	case_122	M	33	focal isolated dystonia (tremulous cervical dystonia	negative	mutational recurrence at codon-51 in gene with missense Z score ≥ 2.0
Autosomal-dominant	*SLC40A1*	0.98	1.77	MIM606069	c.469G>C	p.Asp157His	missense	not found; not found	not found	31	case_088	F	44	focal isolated dystonia (cervical dystonia)	positive	mutational recurrence at codon-157, a site previously associated with hemochromatosis 4

Sex: M = male, F = female. ExAC = exome aggregation consortium, Cambridge, MA (http://exac.broadinstitute.org). pLI = probability of being loss-of-function intolerant. OMIM = Online Mendelian Inheritance in Man (https://omim.org/). CADD = Combined Annotation Dependent Depletion.

[a]numbering according to NCBI accessions NM_003787.4 and NP_003778.2 for *NOL4*, NM_001029858.3 and NP_001025029.2 for *SLC35F1*, NM_014585.5 and NP_055400.1 for *SLC40A1*, and NM_006931.2 and NP_008862.1 for *SLC2A3*.

[b]consisting of roughly 10,000 non-dystonia control exomes.

we analyzed two additional murine datasets of KMT2B-vulnerable genes from brain neurons (Kerimoglu et al., 2013) and ESCs (Denissov et al., 2014), respectively (Table S3), scoring them against the same panel of 225 exomes from dystonia patients. We found that the deletion of *Kmt2b* in these different cellular systems led to the identification of different targets and that the percentage of candidate dystonia-causative genes was different in the three cellular types. Specifically, the percentage of dystonia candidate genes was significantly higher in the iN versus ESC set of KMT2B targets for pLi score (Table S4), suggesting that transdifferentiation uncovers greater vulnerability in the KMT2B-dependent pathways at play in dystonia.

DISCUSSION

Here, we showed that KMT2B is required for the BAM-mediated epigenome remodeling that underlies the MEF-to-iN conversion and that the molecular unravelling of this phenotype exposes dystonia candidate genes. In particular, we demonstrated, for KMT2B, a dual role in the promotion of iN conversion through suppression of the alternative myocytic fate as well as in iN maturation. In contrast, KMT2A proved dispensable and, despite being a paralog of KMT2B, was unable to replace it in transdifferentiation. Beyond identification of the first chromatin regulator essential for MEF-to-iN conversion, our findings support the following conclusions about the specificity of direct neuronal programming.

First, the requirement for KMT2B in iN generation only partially recapitulates its function during both *in vitro* and *in vivo* neuronal differentiation. *In vitro*, *Kmt2b*$^{-/-}$ ESCs present an impaired differentiation to neurons (Lubitz et al., 2007), whereas the deletion of *Kmt2b* in excitatory forebrain terminally differentiated neurons did not impinge brain morphology macroscopically but impaired memory formation and affected H3K4me3 deposition (Kerimoglu et al., 2013, 2017). This notwithstanding, we found high convergence in vulnerable H3K4me3 sites upon loss of KMT2B between *in vivo* matured neurons and transdifferentiated iNs. Conversely, the dispensability of KMT2A in MEF transdifferentiation stands in stark contrast with its essential role during neuronal differentiation, as observed both in murine SVZ (Lim et al., 2009) and in *D. rerio* (Huang et al., 2015). Together, these results highlight how different origins and/or transition paths to similar developmental endpoints (namely, transdifferentiation and differentiation) expose distinct epigenetic requirements. This, in turn, has major implications for the choice of programming or reprogramming paradigms in disease modeling and regeneration, especially when they are intended to model or remedy deficits in epigenetic regulation.

Second, we previously showed that the defective response to lipopolysaccharide (LPS) in *Kmt2b*$^{-/-}$ macrophages was imputable to a single downstream gene, *Pigp*, which aberrantly accumulated H3K27me3 (Austenaa et al., 2012). In MEF-to-iN transition, instead, we found that loss of KMT2B leads to massive transcriptional dysregulation and H3K4me3 redistribution that affects, starting already at the MEF level, the whole program of iN fate acquisition and maturation rather than specific master regulators, pointing to distinct logics of cell fate control downstream of the same chromatin modifier.

Third, the presence of H3K4me3 at lineage-specific genes has been recently proposed as a molecular roadblock to reprogramming in the nuclear transfer (NT) paradigm (Hörmanseder et al., 2017), leading to a model in which H3K4me3-dependent memory of transcriptional status in donor cells limits the reprogramming of their developmental potential. H3K4me3 inhibition in somatic cells thus favors their reacquisition of pluripotency but disables their ability to undergo inter-lineage cell conversion. Because the H3K4me3 inhibition upon NT was carried out by overexpressing the H3K4 demethylase *Kdm5b*, likely its global effects are neither directly comparable with nor symmetrical to our setting, in which the bulk H3K4me3 axis (operated by KMT2E and KMT2F) was left intact. It is worth noting, however, that inhibition of H3K4 demethylase LSD1 (KDM1A) promotes TF-induced reprogramming to pluripotency (Cacchiarelli et al., 2015). Thus, this symmetrical convergence with our findings points to a fundamental distinction in how NT- versus TF-based reprogramming handles H3K4me3 dynamics.

Finally, our work innovatively exploited transdifferentiation as a tool for the identification and prioritization of candidate causative variants. Because *KMT2B* loss-of-function mutations lead to dystonia (Meyer et al., 2017; Zech et al., 2016), we reasoned that the KMT2B-vulnerable targets exposed through the MEF-to-iN transition could guide our search for dystonia-relevant variants and genes in whole-exome sequences of dystonia patients. Indeed, we found, in 39 KMT2B targets, 45 unique protein-impactful alterations, including mutations in 3 promising candidates: *NOL4*, *SLC35F1*, and *SLC40A1*. *NOL3*, notable for its relationship to *NOL4*, has been previously associated with myoclonus (Russell et al., 2012), whereas for *SLC35F1*, we found a mutational recurrence at the same codon in 2 probands with very similar phenotypes. Finally, for *SLC40A1*, we scored a mutational recurrence at a codon previously associated with hemochromatosis type 4 and, therefore, with iron deposition. The proband was found to have elevated serum ferritin and possibly iron deposits on brain MRI (bilateral signal alterations of basal ganglia), in line with signal alterations of basal ganglia described in most *KMT2B*-mutated patients (Meyer et al., 2017) that had not yet been associated with iron deposits, raising the intriguing possibility that the brain signal alterations seen in KMT2B probands might be due to iron abnormalities induced by SLC40A1-mediated downstream effects. Together, these data offer a compendium of promising candidates that are now opened up for further validation, following the recent trend in human genomics in which mutations originally uncovered in single individuals are eventually consolidated in the definition of syndromes (Vissers et al., 2010; Gabriele et al., 2017).

EXPERIMENTAL PROCEDURES

MEF Derivation

MEFs were derived from mice with cKO for *Kmt2a* (Kranz et al., 2010), *Kmt2b* (Glaser et al., 2006), or both methylases and housed and bred in a specific pathogen-free animal house. Control MEFs were derived from *Kmt2a*$^{+/+}$*YFP*$^{+}$ *Cre*$^{+}$ embryos and, in the case of *Kmt2a*, also from *Kmt2a*$^{fl/+}$*YFP*$^{+}$*Cre*$^{+}$ ones. See the Supplemental Experimental Procedures for further details.

Mouse Experiments

Experiments involving animals were carried out in accordance with the Italian Law (D.lgs. 26/2014) that enforces Directive 2010/63/EU of the European

Parliament and of the Council of 22 September 2010, on the protection of animals used for scientific purposes. The project started before the passing of D.lgs. 26/2014 and was thus notified to the Ministry of Health before the implementation of the current legislation. As the new legislation does not apply to projects approved before its enactment, for such projects only a notification of the experiments to the Ministry of Health was required (in accordance with the D.L.vo 116/92 [and following additions], which enforced EU 86/609 Directive), and this requirement was dutifully fulfilled. Following the coming into force of Italian Law (D.lgs. 26/2014) and the expiration of the previously notified project, we submitted for the continuation of the project a new application to the Ministry of Health that granted us the authorization under Project n 385/2016.

Immunofluorescence

MEFs were seeded with different cell densities in Nunc Lab-Tek Permanox chamber slides (Sigma-Aldrich) in duplicates. 3 and 13 days after plating for transduction, cells were stained and acquired with a BX61 upright microscope equipped with a motorized stage from Olympus. The software ScanR (Olympus) was used, and the objective utilized was 20× with a 0.75 numerical aperture. See the Supplemental Experimental Procedures for further details.

Cytofluorimetric Analysis

The PSA-NCAM antibody used is listed in Table S7. 3 min before each tube was acquired, 5–10 μL of propidium iodide (PI) (Sigma-Aldrich, P4170-1G) was added. Samples were acquired at BD FacsCalibur with the BD CellQuest Pro software and analyzed with the Flowjo software. Unpaired t test was executed. See the Supplemental Experimental Procedures for further details.

FACS

FACS was executed on 4-OHT-treated MEFs left in culture 7 days before transdifferentiation. MEFs were plated on Matrigel-coated dishes both for RNA-seq and the ChIP-seq on iNs at 13 days. Cells were sorted for PSA-NCAM positivity at MoFlo Astrios (Beckman Coulter) with the software Summit v6.2. The negative PSA-NCAM fraction was kept as well.

RNA-Seq

RNA was extracted with the RNeasy micro kit (QIAGEN). RNA quality was evaluated with the Agilent 2100 Bioanalyzer. Total RNA was depleted of rRNA with Ribo-Zero, and libraries were prepared with the TruSeq Stranded Total RNA Sample Preparation Kit (Illumina) starting from 100 ng of RNA per sample and sequenced with the Illumina HiSeq machine at a read length of 100 bp, paired ends, and a coverage of 120 million reads. See the Supplemental Experimental Procedures for further details.

ChIP-Seq

ChIP-seq for MENIN was performed on bulk 5-day transdifferentiating MEFs, ChIP-seq for H3K4me3 on MEFs 2 and 7 days after the last 4-OHT administration, on the whole-cell population at 5 days, and on PSA-NCAM$^+$ cells at 13 days. H3K27me3 ChIP-seq was performed on MEFs 2 and 7 days after the last 4-OHT administration and on the whole-cell population at 5 days. See the Supplemental Experimental Procedures for further details.

Exome Analysis

WES and analysis of all 225 dystonia subjects was performed as described previously (Zech et al., 2016, 2017). Assuming that causative mutations in the proband cohort are coding alleles of strong effect, we searched the full WES dataset for missense, in-frame insertion or deletion (indel), stop-gain and stop-loss, frameshift, and splice site variations in any of the KMT2B-sensitive genes (Figure S6A). Filtered variants were considered under both an autosomal dominant (1 heterozygous variant per gene per proband) and an autosomal recessive disease model (homozygous variant or 2 heterozygous variants per gene per proband). See the Supplemental Experimental Procedures for further details.

Ethics Approval

Recruitment of dystonia patients and genetic analyses were performed after approval by the local ethics review boards at each participating center. All dystonia patients provided written informed consent.

DATA AND SOFTWARE AVAILABILITY

The accession number for the sequencing data reported in this paper is GEO: GSE120441.

SUPPLEMENTAL INFORMATION

Supplemental Information includes Supplemental Experimental Procedures, six figures, and eight tables and can be found with this article online at https://doi.org/10.1016/j.celrep.2018.09.067.

ACKNOWLEDGMENTS

This work was supported by European Research Council (ERC) grant DISEASEAVATARS #616441 (to G.T.), the EPIGEN Flagship Project of the Italian National Research Council (CNR) (to G.T.), ERANET-Neuron grants from the Italian Ministry of Health (FoodForThought - F4T to G.T. and AUTSYN to P.-L.G.), Associazione Italiana per la Ricerca sul Cancro (AIRC) (IG to G.T.), Regione Lombardia (Ricerca Indipendente 2012 to G.T.), the Umberto Veronesi Foundation (to P.L.-G. and S.A.), the Italian Ministry of Health (Ricerca Corrente grant to G.T.), Fondazione Italiana per la Ricerca sul Cancro (FIRC) (to P.L.R.), and the European Research Council (AdERC #340527 to V.B.). Recruitment of dystonia patients and genetic analyses were funded by a research grant from the Else Kröner-Fresenius-Stiftung as well as in-house institutional funding from Technische Universität München (Munich, Germany), Helmholtz Zentrum München (Munich, Germany), and Medizinische Universität Innsbruck (Innsbruck, Austria) as well as Czech Science Foundation grant GACR16-13323S and Charles University (Prague, Czech Republic) project Progres Q27/LF1.

AUTHOR CONTRIBUTIONS

G.B. carried out all experiments, including animal crossing, MEF derivation and transdifferentiation, ScanR imaging analysis, FACS acquisition and analyses, qRT-PCR, and ChIP-seq. P.-L.G. performed RNA-seq and ChIP-seq analyses. M.Z. and J.W. analyzed KMT2B targets in exomes of dystonia patients. S.A. initiated the project, set up the transdifferentiation protocol, derived some MEFs of this study, and maintained colonies before G.B.'s arrival. G.B. and P.L.R. carried out BAM vector production. A.D.-C. imported the colonies and designed primers for exon 2 copy numbers. G.B., P.L.R., and E.T. carried out RNA-seq library preparation. S.B., B.H., and R.J. recruited dystonia patients. A.F.S. shared the mice and the antibody for KMT2B. M.C. and V.B. shared the transdifferentiation protocol. G.B., P.-L.G., P.L.R., and G.T. wrote the paper. G.T. conceived, designed, and supervised the study.

DECLARATION OF INTERESTS

The authors declare no competing interests.

Received: December 27, 2017
Revised: August 1, 2018
Accepted: September 19, 2018
Published: October 23, 2018

REFERENCES

Austenaa, L., Barozzi, I., Chronowska, A., Termanini, A., Ostuni, R., Prosperini, E., Stewart, A.F., Testa, G., and Natoli, G. (2012). The histone methyltransferase Wbp7 controls macrophage function through GPI glycolipid anchor synthesis. Immunity *36*, 572–585.

Cacchiarelli, D., Trapnell, C., Ziller, M.J., Soumillon, M., Cesana, M., Karnik, R., Donaghey, J., Smith, Z.D., Ratanasirintrawoot, S., Zhang, X., et al. (2015). Integrative Analyses of Human Reprogramming Reveal Dynamic Nature of Induced Pluripotency. Cell *162*, 412–424.

Callebaut, I., Joubrel, R., Pissard, S., Kannengiesser, C., Gérolami, V., Ged, C., Cadet, E., Cartault, F., Ka, C., Gourlaouen, I., et al. (2014). Comprehensive

functional annotation of 18 missense mutations found in suspected hemochromatosis type 4 patients. Hum. Mol. Genet. *23*, 4479–4490.

Chronis, C., Fiziev, P., Papp, B., Butz, S., Bonora, G., Sabri, S., Ernst, J., and Plath, K. (2017). Cooperative Binding of Transcription Factors Orchestrates Reprogramming. Cell *168*, 442–459.e20.

Denissov, S., Hofemeister, H., Marks, H., Kranz, A., Ciotta, G., Singh, S., Anastassiadis, K., Stunnenberg, H.G., and Stewart, A.F. (2014). Mll2 is required for H3K4 trimethylation on bivalent promoters in embryonic stem cells, whereas Mll1 is redundant. Development *141*, 526–537.

Ernst, P., Fisher, J.K., Avery, W., Wade, S., Foy, D., and Korsmeyer, S.J. (2004). Definitive hematopoiesis requires the mixed-lineage leukemia gene. Dev. Cell *6*, 437–443.

Gabriele, M., Vulto-van Silfhout, A.T., Germain, P.L., Vitriolo, A., Kumar, R., Douglas, E., Haan, E., Kosaki, K., Takenouchi, T., Rauch, A., et al. (2017). YY1 Haploinsufficiency Causes an Intellectual Disability Syndrome Featuring Transcriptional and Chromatin Dysfunction. Am. J. Hum. Genet. *100*, 907–925.

Glaser, S., Schaft, J., Lubitz, S., Vintersten, K., van der Hoeven, F., Tufteland, K.R., Aasland, R., Anastassiadis, K., Ang, S.L., and Stewart, A.F. (2006). Multiple epigenetic maintenance factors implicated by the loss of Mll2 in mouse development. Development *133*, 1423–1432.

Hetet, G., Devaux, I., Soufir, N., Grandchamp, B., and Beaumont, C. (2003). Molecular analyses of patients with hyperferritinemia and normal serum iron values reveal both L ferritin IRE and 3 new ferroportin (slc11A3) mutations. Blood *102*, 1904–1910.

Hörmanseder, E., Simeone, A., Allen, G.E., Bradshaw, C.R., Figlmüller, M., Gurdon, J., and Jullien, J. (2017). H3K4 Methylation-Dependent Memory of Somatic Cell Identity Inhibits Reprogramming and Development of Nuclear Transfer Embryos. Cell Stem Cell *21*, 135–143.e6.

Hu, D., Gao, X., Cao, K., Morgan, M.A., Mas, G., Smith, E.R., Volk, A.G., Bartom, E.T., Crispino, J.D., Di Croce, L., and Shilatifard, A. (2017). Not All H3K4 Methylations Are Created Equal: Mll2/COMPASS Dependency in Primordial Germ Cell Specification. Mol. Cell *65*, 460–475.e6.

Huang, Y.C., Shih, H.Y., Lin, S.J., Chiu, C.C., Ma, T.L., Yeh, T.H., and Cheng, Y.C. (2015). The epigenetic factor Kmt2a/Mll1 regulates neural progenitor proliferation and neuronal and glial differentiation. Dev. Neurobiol. *75*, 452–462.

Hughes, C.M., Rozenblatt-Rosen, O., Milne, T.A., Copeland, T.D., Levine, S.S., Lee, J.C., Hayes, D.N., Shanmugam, K.S., Bhattacharjee, A., Biondi, C.A., et al. (2004). Menin associates with a trithorax family histone methyltransferase complex and with the hoxc8 locus. Mol. Cell *13*, 587–597.

Kerimoglu, C., Agis-Balboa, R.C., Kranz, A., Stilling, R., Bahari-Javan, S., Benito-Garagorri, E., Halder, R., Burkhardt, S., Stewart, A.F., and Fischer, A. (2013). Histone-methyltransferase MLL2 (KMT2B) is required for memory formation in mice. J. Neurosci. *33*, 3452–3464.

Kerimoglu, C., Sakib, M.S., Jain, G., Benito, E., Burkhardt, S., Capece, V., Kaurani, L., Halder, R., Agís-Balboa, R.C., Stilling, R., et al. (2017). KMT2A and KMT2B Mediate Memory Function by Affecting Distinct Genomic Regions. Cell Rep. *20*, 538–548.

Kranz, A., Fu, J., Duerschke, K., Weidlich, S., Naumann, R., Stewart, A.F., and Anastassiadis, K. (2010). An improved Flp deleter mouse in C57Bl/6 based on Flpo recombinase. Genesis *48*, 512–520.

Lee, S., Lee, D.K., Dou, Y., Lee, J., Lee, B., Kwak, E., Kong, Y.Y., Lee, S.K., Roeder, R.G., and Lee, J.W. (2006). Coactivator as a target gene specificity determinant for histone H3 lysine 4 methyltransferases. Proc. Natl. Acad. Sci. USA *103*, 15392–15397.

Lek, M., Karczewski, K.J., Minikel, E.V., Samocha, K.E., Banks, E., Fennell, T., O'Donnell-Luria, A.H., Ware, J.S., Hill, A.J., Cummings, B.B., et al.; Exome Aggregation Consortium (2016). Analysis of protein-coding genetic variation in 60,706 humans. Nature *536*, 285–291.

Lim, D.A., Huang, Y.C., Swigut, T., Mirick, A.L., Garcia-Verdugo, J.M., Wysocka, J., Ernst, P., and Alvarez-Buylla, A. (2009). Chromatin remodelling factor Mll1 is essential for neurogenesis from postnatal neural stem cells. Nature *458*, 529–533.

Lubitz, S., Glaser, S., Schaft, J., Stewart, A.F., and Anastassiadis, K. (2007). Increased apoptosis and skewed differentiation in mouse embryonic stem cells lacking the histone methyltransferase Mll2. Mol. Biol. Cell *18*, 2356–2366.

Mall, M., Kareta, M.S., Chanda, S., Ahlenius, H., Perotti, N., Zhou, B., Grieder, S.D., Ge, X., Drake, S., Euong Ang, C., et al. (2017). Myt1l safeguards neuronal identity by actively repressing many non-neuronal fates. Nature *544*, 245–249.

Meyer, E., Carss, K.J., Rankin, J., Nichols, J.M., Grozeva, D., Joseph, A.P., Mencacci, N.E., Papandreou, A., Ng, J., Barral, S., et al.; UK10K Consortium; Deciphering Developmental Disorders Study; NIHR BioResource Rare Diseases Consortium (2017). Mutations in the histone methyltransferase gene KMT2B cause complex early-onset dystonia. Nat. Genet. *49*, 223–237.

Pinney, D.F., Pearson-White, S.H., Konieczny, S.F., Latham, K.E., and Emerson, C.P., Jr. (1988). Myogenic lineage determination and differentiation: evidence for a regulatory gene pathway. Cell *53*, 781–793.

Russell, J.F., Steckley, J.L., Coppola, G., Hahn, A.F., Howard, M.A., Kornberg, Z., Huang, A., Mirsattari, S.M., Merriman, B., Klein, E., et al. (2012). Familial cortical myoclonus with a mutation in NOL3. Ann. Neurol. *72*, 175–183.

Strom, S.P., Lozano, R., Lee, H., Dorrani, N., Mann, J., O'Lague, P.F., Mans, N., Deignan, J.L., Vilain, E., Nelson, S.F., et al. (2014). De Novo variants in the KMT2A (MLL) gene causing atypical Wiedemann-Steiner syndrome in two unrelated individuals identified by clinical exome sequencing. BMC Med. Genet. *15*, 49.

Testa, G., Schaft, J., van der Hoeven, F., Glaser, S., Anastassiadis, K., Zhang, Y., Hermann, T., Stremmel, W., and Stewart, A.F. (2004). A reliable lacZ expression reporter cassette for multipurpose, knockout-first alleles. Genesis *38*, 151–158.

Treutlein, B., Lee, Q.Y., Camp, J.G., Mall, M., Koh, W., Shariati, S.A., Sim, S., Neff, N.F., Skotheim, J.M., Wernig, M., and Quake, S.R. (2016). Dissecting direct reprogramming from fibroblast to neuron using single-cell RNA-seq. Nature *534*, 391–395.

Vierbuchen, T., Ostermeier, A., Pang, Z.P., Kokubu, Y., Südhof, T.C., and Wernig, M. (2010). Direct conversion of fibroblasts to functional neurons by defined factors. Nature *463*, 1035–1041.

Vissers, L.E., de Ligt, J., Gilissen, C., Janssen, I., Steehouwer, M., de Vries, P., van Lier, B., Arts, P., Wieskamp, N., del Rosario, M., et al. (2010). A de novo paradigm for mental retardation. Nat. Genet. *42*, 1109–1112.

Wapinski, O.L., Vierbuchen, T., Qu, K., Lee, Q.Y., Chanda, S., Fuentes, D.R., Giresi, P.G., Ng, Y.H., Marro, S., Neff, N.F., et al. (2013). Hierarchical mechanisms for direct reprogramming of fibroblasts to neurons. Cell *155*, 621–635.

Wapinski, O.L., Lee, Q.Y., Chen, A.C., Li, R., Corces, M.R., Ang, C.E., Treutlein, B., Xiang, C., Baubet, V., Suchy, F.P., et al. (2017). Rapid Chromatin Switch in the Direct Reprogramming of Fibroblasts to Neurons. Cell Rep. *20*, 3236–3247.

Zech, M., Boesch, S., Maier, E.M., Borggraefe, I., Vill, K., Laccone, F., Pilshofer, V., Ceballos-Baumann, A., Alhaddad, B., Berutti, R., et al. (2016). Haploinsufficiency of KMT2B, Encoding the Lysine-Specific Histone Methyltransferase 2B, Results in Early-Onset Generalized Dystonia. Am. J. Hum. Genet. *99*, 1377–1387.

Zech, M., Boesch, S., Jochim, A., Weber, S., Meindl, T., Schormair, B., Wieland, T., Lunetta, C., Sansone, V., Messner, M., et al. (2017). Clinical exome sequencing in early-onset generalized dystonia and large-scale resequencing follow-up. Mov. Disord. *32*, 549–559.

Cell Reports, Volume *25*

Supplemental Information

KMT2B Is Selectively Required for Neuronal Transdifferentiation, and Its Loss Exposes Dystonia Candidate Genes

Giulia Barbagiovanni, Pierre-Luc Germain, Michael Zech, Sina Atashpaz, Pietro Lo Riso, Agnieszka D'Antonio-Chronowska, Erika Tenderini, Massimiliano Caiazzo, Sylvia Boesch, Robert Jech, Bernhard Haslinger, Vania Broccoli, Adrian Francis Stewart, Juliane Winkelmann, and Giuseppe Testa

***Kmt2b* cKO (plated 7 days after 4-OHT)**

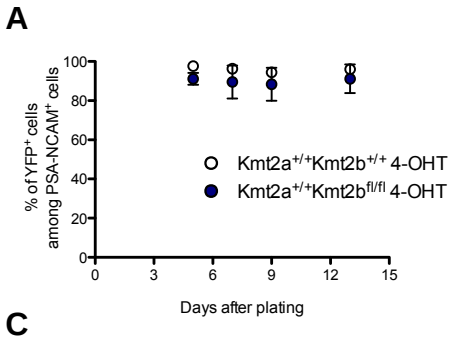

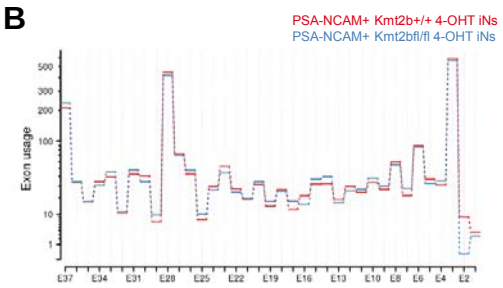

***Kmt2a* cKO: ScanR (plated 2 days after 4-OHT)**

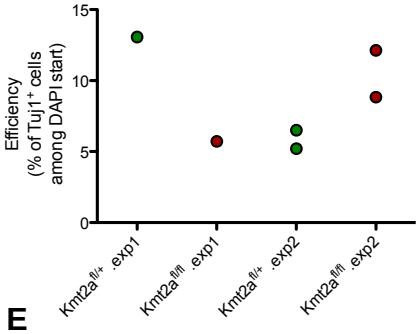

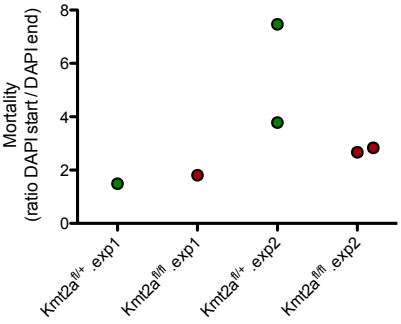

***Kmt2a Kmt2b* cKO before transdifferentiation**

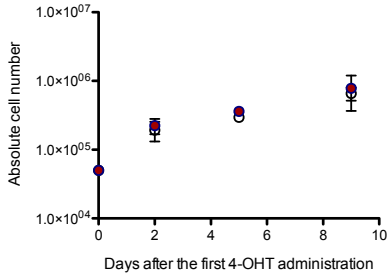

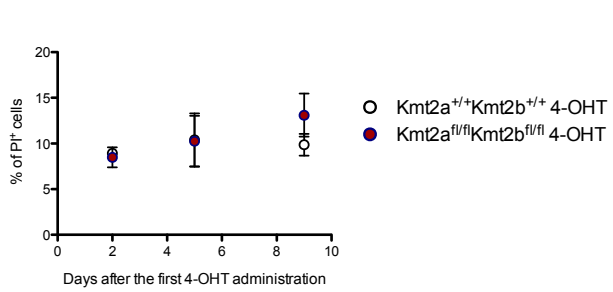

***Kmt2a* cKO: FACS (plated 7 days after 4-OHT)**

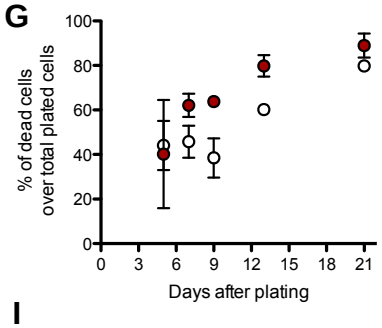

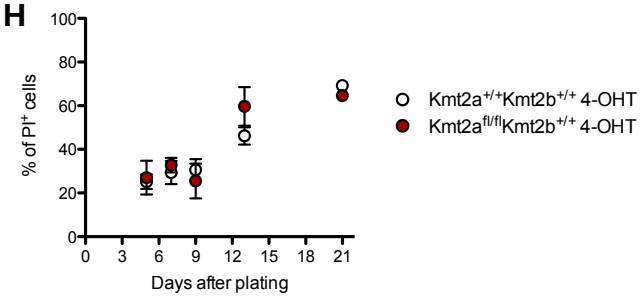

***Kmt2b* cKO FACS (plated 7 days after 4-OHT)**

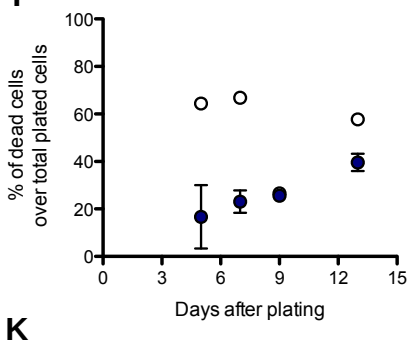

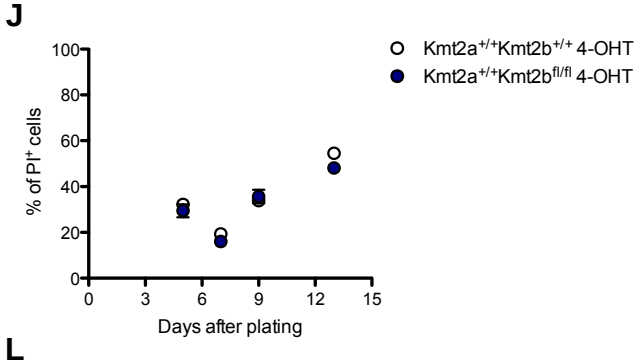

***Kmt2a Kmt2b* cKO: FACS (plated 7 days after 4-OHT)**

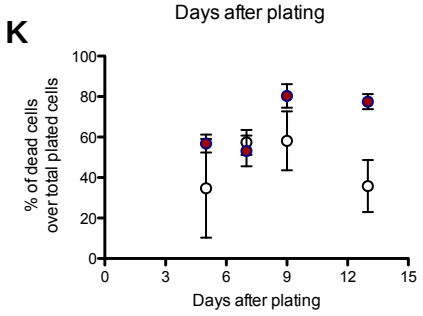

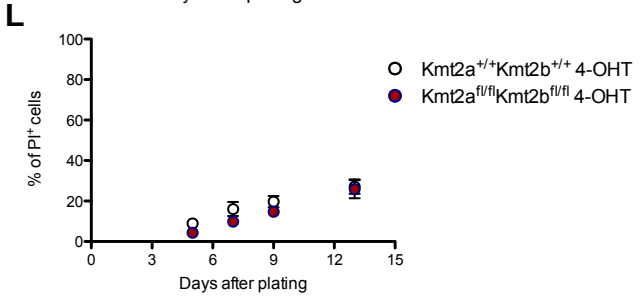

Figure S1. The role of KMT2A and KMT2B during transdifferentiation, related to Figure 2

A, Percentage of YFP$^+$ cells among PSA-NCAM$^+$ cells 5, 7, 9 and 13 days after plating in *Kmt2a*$^{+/+}$*Kmt2b*$^{+/+}$ (n=2) and *Kmt2a*$^{+/+}$*Kmt2b*$^{fl/fl}$ (n=2) 4-OHT transdifferentiating MEFs. **B,** The graph shows *Kmt2b* exon usage in *Kmt2b*$^{fl/fl}$ (in blue) and *Kmt2b*$^{+/+}$ (in red) 4-OHT treated 13-days sorted iNs obtained through RNA-seq analysis. **C,** Efficiency of transdifferentiation in ScanR experiments calculated relating the number of Tuj1$^+$ at 13 days, of the chosen concentration, to the number of DAPI 3 days after plating. **D,** Cell mortality in ScanR experiments calculated as the ratio of DAPI 3 days (DAPI start) and 13 days (DAPI end) after plating. In **C-D**, 2 independent experiments (exp1 and exp2) were performed and cells were plated 2 days after the last 4-OHT administration. **E,** Percentage of dead cells was calculated over the initial number of plated MEFs 2, 5 and 9 days after the first 4-OHT administration. **F**, Mortality rate as percentage of PI$^+$ cells 2, 5 and 9 days after the first 4-OHT administration. **E-F** *Kmt2a*$^{+/+}$ *Kmt2b*$^{+/+}$ n=5; *Kmt2a*$^{fl/fl}$ *Kmt2b*$^{fl/fl}$ n=3. **G, I, K,** Percentage of dead cells was calculated over the initial number of plated MEFs. (G) *Kmt2a*$^{fl/fl}$ n=3; *Kmt2a*$^{+/+}$ n=3 at all time points, but day 21: n=2. (I) *Kmt2a*$^{+/+}$ *Kmt2b*$^{+/+}$ n=1; *Kmt2a*$^{+/+}$ *Kmt2b*$^{fl/fl}$ n=2 despite day 9 n=1. (K) *Kmt2a*$^{+/+}$ *Kmt2b*$^{+/+}$ n=3; *Kmt2a*$^{fl/fl}$ *Kmt2b*$^{fl/fl}$ n=3. **H, J, L,** Mortality rate as percentage of PI$^+$ cells 5, 7, 9, 13 (and 21 for (H)) days after plating, assayed with FACS analysis. (H) *Kmt2a*$^{fl/fl}$ n=3 at all time points, but day 21 in which n=2; *Kmt2a*$^{+/+}$ n=3 at all time points, but day 21 in which n=1. (J) *Kmt2a*$^{+/+}$ *Kmt2b*$^{+/+}$ n=1; *Kmt2a*$^{+/+}$ *Kmt2b*$^{fl/fl}$ n=2. (L) *Kmt2a*$^{+/+}$ *Kmt2b*$^{+/+}$ n=3; *Kmt2a*$^{fl/fl}$ *Kmt2b*$^{fl/fl}$ n=3. **A-L,** Error bars show means +/- SEM. **A**-**B**, **G**-**L**, MEFs were plated for transdifferentiation 7 days after the end of 4-OHT treatment.

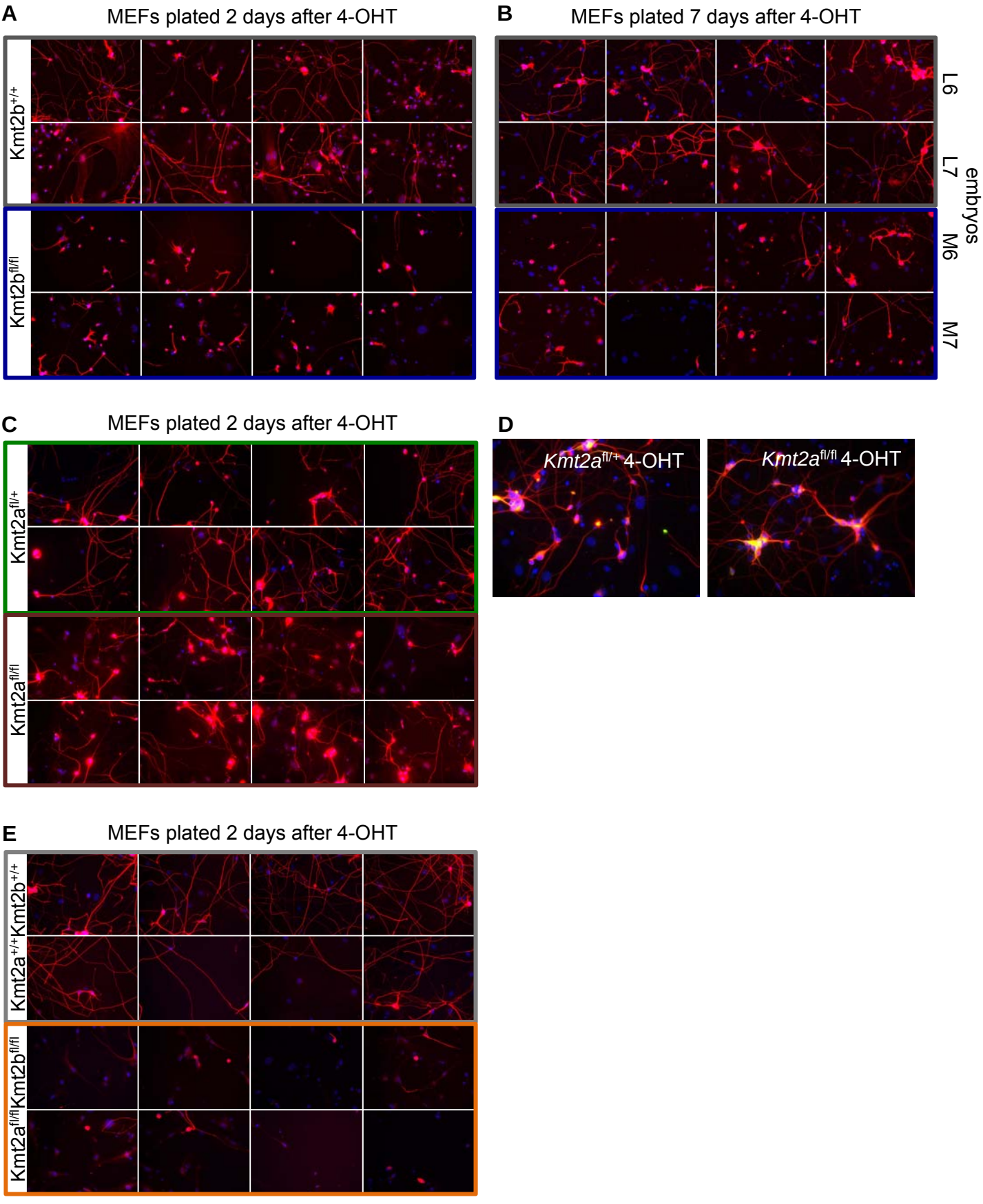
A
MEFs plated 2 days after 4-OHT
Kmt2b+/+
Kmt2bfl/fl
B
MEFs plated 7 days after 4-OHT
L6
L7
M6
M7
embryos
C
MEFs plated 2 days after 4-OHT
Kmt2afl/+
Kmt2afl/fl
D
Kmt2afl/+ 4-OHT
Kmt2afl/fl 4-OHT
E
MEFs plated 2 days after 4-OHT
Kmt2a+/+Kmt2b+/+
Kmt2afl/flKmt2bfl/fl

Figure S2. KMT2B is fundamental for iN maturation while KMT2A is dispensable, related to Figure 2

Representative images of *Kmt2b*$^{fl/fl}$ and *Kmt2b*$^{+/+}$ 4-OHT transdifferentiated MEFs at 13 days, plated either 2 (**A**) or 7 (**B**) days after 4-OHT, of *Kmt2a*$^{fl/fl}$ and *Kmt2a*$^{fl/+}$ (used as control instead of *Kmt2a*$^{+/+}$) 4-OHT transdifferentiated MEFs at 13 days, plated 2 days after 4-OHT (**C**) and of *Kmt2a*$^{+/+}$*Kmt2b*$^{+/+}$ and *Kmt2a*$^{fl/fl}$ *Kmt2b*$^{fl/fl}$ 4-OHT transdifferentiated MEFs at 13 days, plated 2 days after 4-OHT (**E**). The grid of images built for KO and ctrl was the same. Images taken in the same areas of the well are reported for cKOs and control. DAPI is in blue and Tuj1 in red. **D,** Representative images of *Kmt2a*$^{fl/+}$ (used as alternative control to *Kmt2a*$^{+/+}$) (left panel) and $^{fl/fl}$ (right panel) 4-OHT treated iNs (DAPI is in blue, Tuj1 in red, MAP2b in green) at 13 days**.**

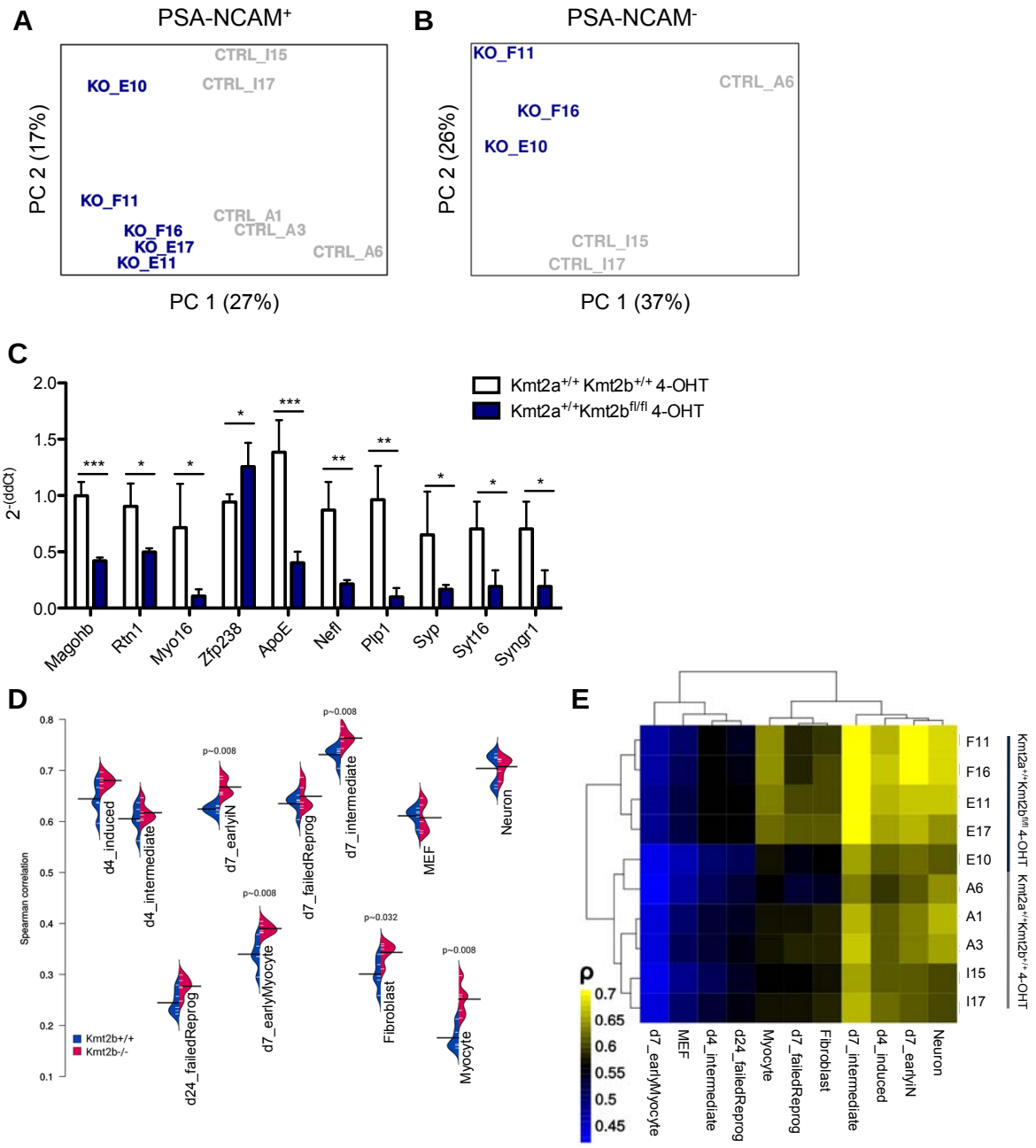

Figure S3. Transcriptomic analysis of PSA-NCAM⁺ cells, related to Figure 3

A, PCA on the log-normalized read counts of *Kmt2a*$^{+/+}$ *Kmt2b*$^{+/+}$ (CTRL_A1, CTRL_A3, CTRL_A6, CTRL_I15, CTRL_I17) and *Kmt2b*$^{-/-}$ (KO_F16, KO_F11, KO_F17, KO_E10, KO_E11) transcriptomes of sorted PSA-NCAM⁺ cells at 13 days. **B,** PCA on the log-normalized read counts of *Kmt2a*$^{+/+}$ *Kmt2b*$^{+/+}$ (CTRL_A6, CTRL_I15, CTRL_I17) and *Kmt2b*$^{-/-}$ (KO_F16, KO_F11, KO_E10) transcriptomes of sorted PSA-NCAM⁻ cells at 13 days. **C**, Validation through RT-qPCR of some of the genes differentially expressed with an impact on the *in vitro* phenotype. Error bars show means and SD. *** p<0.0001; ** p<0.001; *p<0.01. Spearman (**D**) and Pearson (**E**) correlation of the *Kmt2b* cKO and control iNs transcriptomes *vis à vis* the different previously reported fates of single cells undergoing transdifferentiation (Treutlein et al., 2016). A1, A3, A6, I15, I17 and E11, E17, E10, F11, F16 are the names of the embryos from where *Kmt2a*$^{+/+}$*Kmt2b*$^{+/+}$ and *Kmt2a*$^{+/+}$*Kmt2b*$^{fl/fl}$ MEFs were derived, respectively.

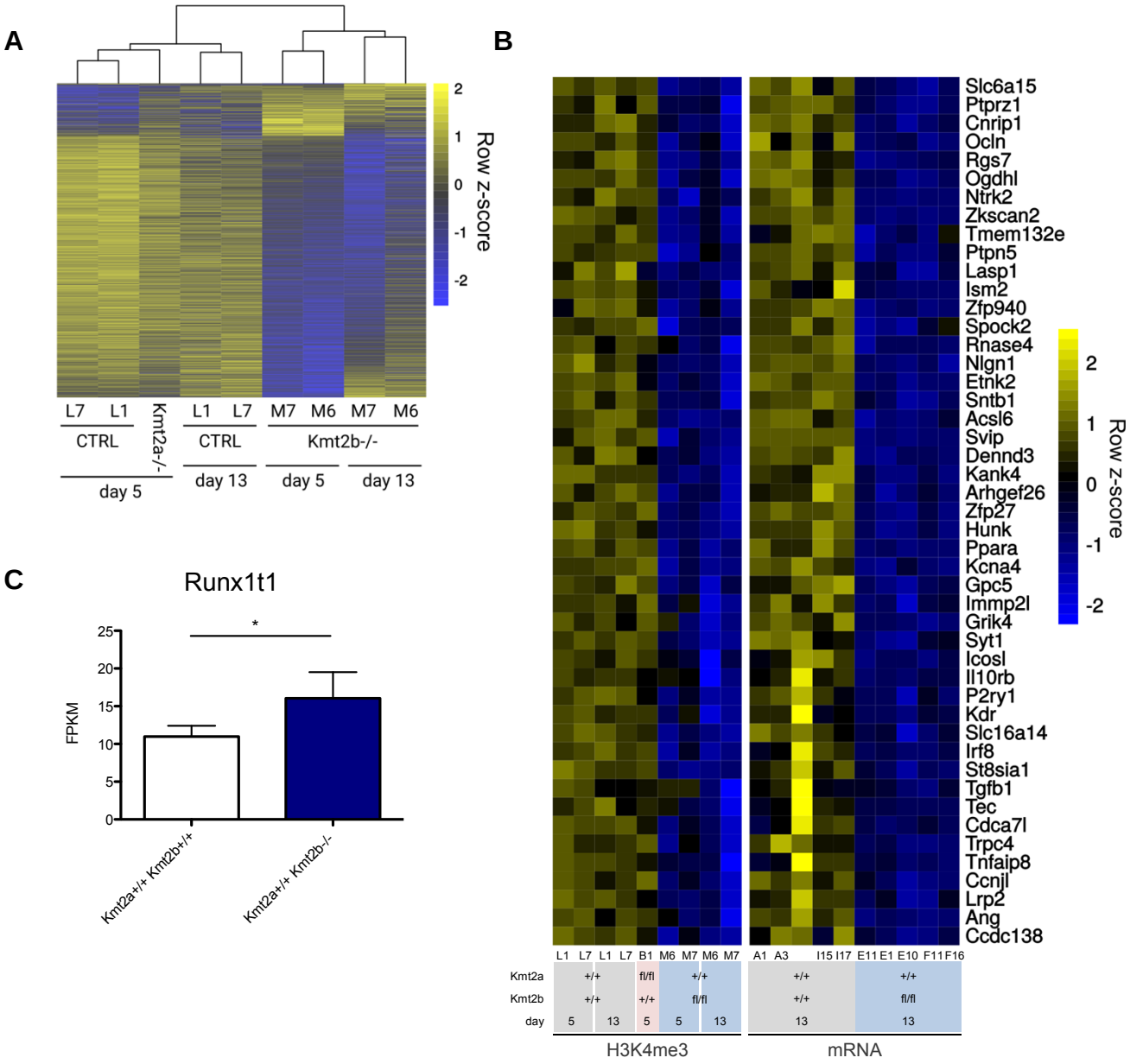

Figure S4. Epigenomic and transcriptomic dissection, related to Figure 6

A, Union of *loci* showing significant changes in H3K4me3 in *Kmt2b* cKO at day 5 and/or 13. **B,** Heatmap of the genes that further lose H3K4 trimethylation in *Kmt2b* cKO samples at 13 days and their expression in RNA-seq at 13 days. **C,** FPKM of *Runx1t1* in our RNA-seq * FDR<0.01**.** Error bars show means and SD. A1, A3, A6, I15, I17, L1, L6, L7 and E11, E17, E10, F11, F16, M6, M7 are the names of the embryos from where *Kmt2a*$^{+/+}$*Kmt2b*$^{+/+}$ and *Kmt2a*$^{+/+}$*Kmt2b*$^{fl/fl}$ MEFs were derived, respectively. B1 is the name of the embryo from where *Kmt2a*$^{fl/fl}$*Kmt2b*$^{+/+}$ MEFs were derived.

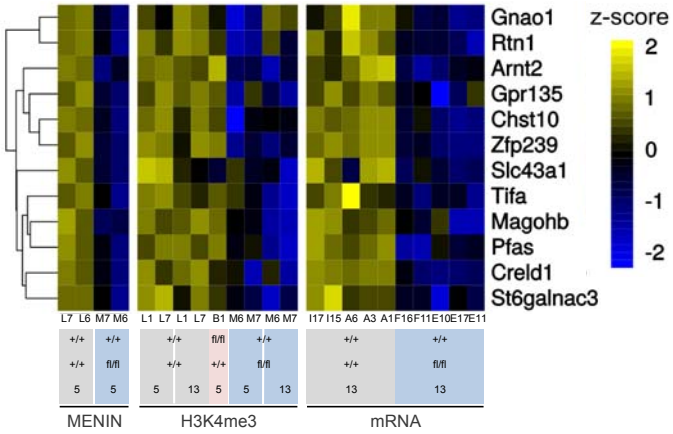

Figure S5. Identification of KMT2B candidate targets through MENIN ChIPseq, related to Figure 6

Heatmap showing the genes both differentially bound by MENIN, differentially expressed (FDR <0.01 and a FC > 0.5) and differentially H3K4me3 in *Kmt2b*$^{-/-}$ with respect to control. A1, A3, A6, I15, I17, L6, L7, L1 and E11, E17, E10, F11, F16, M6, M7 are the names of the embryos from where *Kmt2a*$^{+/+}$*Kmt2b*$^{+/+}$ and *Kmt2a*$^{+/+}$*Kmt2b*$^{fl/fl}$ MEFs were derived, respectively. B1 is the name of the embryo from which *Kmt2a*$^{fl/fl}$ MEFs were derived.

A

Variant calls in 216 *KMT2B*-target genes
across 225 dystonia samples

↓

High-confidence calls
read depth >20x, quality score >30 (Phred scale)

↓

Non-silent variation in canonical transcripts
missense, in-frame indel, loss-of-function (stop-gain/lost, frameshift, splice-site) variants in NCBI RefSeq variant 1 transcripts

↓

Frequency filter

Autosomal-dominant disease model[a] variants not represented in ExAC and in-house control databases[c]		**Autosomal-recessive disease model**[b] variants with minor allele frequency <0.001 in ExAC and in-house control databases[c]	
Predicted damaging missense and in-frame indel variants (CADD score ≥ 20)[d]	**Loss-of-function variants**	**Predicted damaging missense and in-frame indel variants** (CADD score ≥ 10)[d]	**Loss-of-function variants**

[a]Single heterozygous variant per gene per sample

[b]Homozygous variant or two heterozygous variants per gene per sample

[c]in-house database consisting of roughly 10,000 non-dystonia control exomes

[d]Scores ≥20 predict that variants are among the 1% most deleterious changes that can affect the human genome, scores ≥10 predict that variants are among the 10% most deleterious

B **SLC35F1**

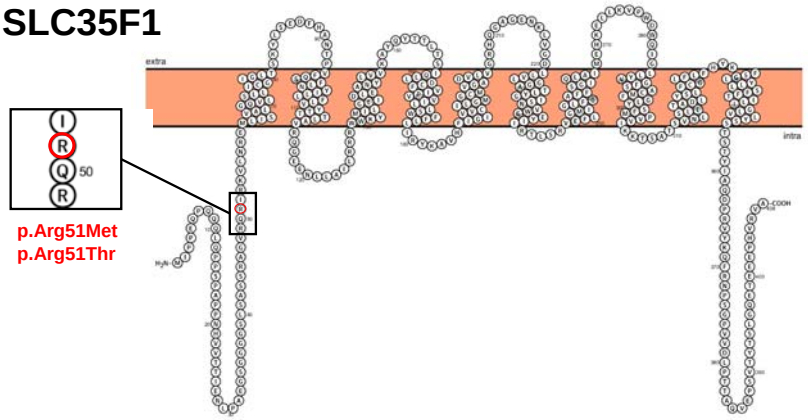

C **SLC40A1**

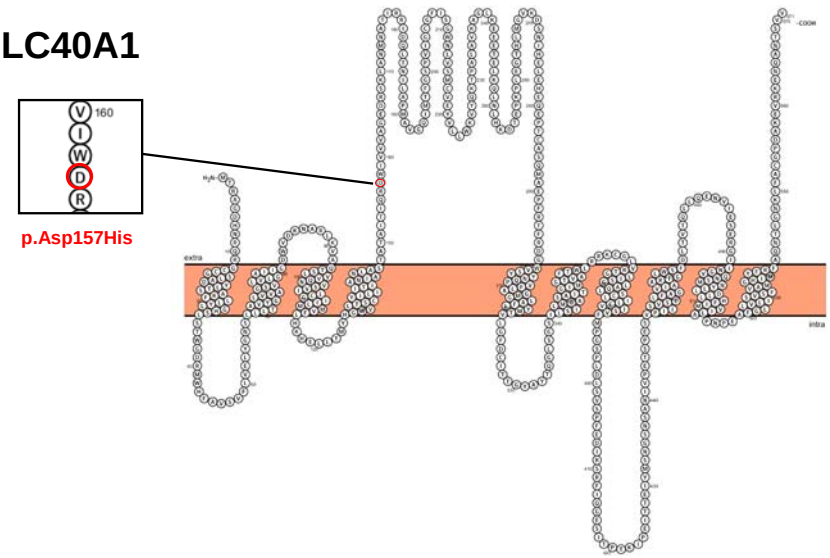

Figure S6. Identification of new putative dystonia-causing variants and genes, related to Table 1

A, Experimental pipeline of variant calling and filtering. **B-C,** Schematics of SLC35F1 and SLC40A1 mutations generated with Protter: interactive protein feature visualization and integration with experimental proteomic data **(Omasits et al., 2014)**.

	Kmt2b fl/fl Vs. +/+		*Kmt2a* fl/fl Vs. fl/+	*Kmt2b* fl/fl *Kmt2a* fl/fl Vs. +/+	
Days after 4-OHT	2	7	2	2	7
N of indipendent embryos per experiment per genotype	1	2	1	1	1
N of indipendent experiments	2	1	2	1	1
N of fields per embryo	100	100	100	100	100
Increased mortality in KO	X	X	1 out of 2	✓	✓
Reduced transdifferentiation efficiency in KO	X	✓	1 out of 2	✓	✓
Reduced neurite length in KO	✓	✓	X	✓	✓

Table S1. Summary of all experiments performed at ScanR, related to Figure 2

	Number of KMT2B targets	pLI ≥ 0.9	Missense Z score ≥ 2	Both
iNs	216	45 (21%)	54 (25%)	26 (12%)
Brain Neurons	127	5 (4%)	11 (9%)	6 (5%)
ESCs	120	9 (7%)	26 (21%)	12 (10%)

Table S4. Summary of the Tables S1 and S2, related to Table 1. χ^2 test: $p < 0{,}005$ iN vs ESC, pLI: 0,00024; iN vs ESC, misZ: 0,58; iN vs ESC, both 0.7.

No. (sex female/male)	225 (133/92)
Age at sampling[a]	50.4 ± 14.6 (18-88)
Age at onset[a]	29.4 ± 15.1 (1-69)
Early symptom onset (<30 years) (%)	48.0
Family history positive (%)	38.7
Dystonia distribution (%)	
Focal	61.8
Segmental	20.0
Generalized	18.2
Dystonia clinical classification[b] (%)	
Isolated	87.9
Combined	5.6
Complex	6.5

Table S5. Clinical characteristics of 225 dystonia-affected probands sequenced by exome, related to Table 1
[a]Mean age in years ± standard deviation (range); [b]according to Albanese et al., 2013 and Marras et al., 2016

N=	Reads[a]	Mapped reads[a]	Percent[a]	Mapped sequence (Gb)[a]	Target bases > 20x[a]	Average coverage[a]
225	129,920,660 ± 18,380,126 (80,589,549-185,236,854)	129,366,209 ± 18,479,892 (79,579,741-184,924,819)	99.55 ± 0.36 (98.74-99.95)	13.14 ± 2.16 (8.04-27.92)	98.49 ± 0.49 (96.47-99.31)	153.54 ± 22.04 (98.46-264.60)

[a]Mean ± standard deviation (range)

Table S6. Summary of statistics for 225 dystonia exomes, related to Table 1

KMT2B	rabbit	Stewart Lab		1:1000	WB
VINCULIN	mouse	Sigma Aldrich	V9131	1:400	WB
TUJ1	mouse	Covance	MMS-435P	1:400	IF
TUJ1	rabbit	Covance	MRB-435P	1:400	IF
VIMENTIN	mouse	Abcam	ab20346	1:200	IF
MAP2B	mouse	BD Biosciences	610460	1:500	IF
H3K4me3	rabbit	Active motif	39159	1ug Ab each 100 ug Cromatin	ChIP
H3K27me3	rabbit	Cell signaling	9733BF	1ug Ab each 25 ug Cromatin	ChIP
MENIN	rabbit	Abcam	ab31902	1ug Ab each 100 ug Cromatin	ChIP
PSA-NCAM	mouse	Miltenyi	130-093-273		FACS

Table S7. List of antibodies used in the study, related to Experimental Procedures

	Forward	**Reverse**
ApoE	CAATTGCGAAGATGAAGGCTC	TAATCCCAGAAGCGGTTCAG
Magohb	CGGGCATAAGGGCAAGTTT	AATTACTGTTGTTGGCATATGTAAGCTT
Myo16	TGTGTCCAGTTGCCTCATAC	CAGGAGAAAATCAGAAAGGTGC
Nefl	GGGTATGAACGAAGCTCTGG	TCTCAGCTCATTCTCCAGTTTG
Plp1	TCAGCCGCAAAACAGACTAG	CACTCCAAAGAAACACAATCCAG
Rtn1	GTGTGGAGCAACTGGAAAAG	CTCCCGAACACAATCCCAG
Syngr1	GGACAACCCTCTGAACGAAG	CCAATCTGGTACCTCTGGAAG
Syp	TGCAGTGGGTCTTTGCCATCTT	ACTTCGATGTTGAGGGCACTCT
Syt16	TCCATACGTCAAAGTCTTCCTG	TGTCTTGCCACCTAATTCCG
Zfp238	TCTCCACTTTGCATCTGTCTC	TGCTGTGGTCTGGAAACTC

Table S8. Sequences of primers used in RT-qPCR, related to Experimental Procedures

Supplemental Experimental Procedures

MEFs derivation

MEFs were derived from embryos at E13.5. After removal of both the head and the liver, cells were enzymatically and mechanically dissociated through the incubation with trypsin at 37° C, 3% O_2, 5% CO_2 for 30 minutes, pipetting every 10 minutes. Dissociated MEFs were seeded in the medium published in the original paper (Vierbuchen et al., 2010) and cultured at 37 °C, 3% O_2 and 5% CO_2.

Control and cKO MEFs at P1-P3 were treated for 5 days with 4-Hydroxytamoxifen (4-OHT), added to the MEF medium in a final concentration of 1000 ng/ml, and then left either 2 or 7 days in medium not supplemented with 4-OHT.

Transdifferentiation was performed according to the protocol published in the original paper (Vierbuchen et al., 2010).

Mice/MEFs were genotyped using the following primers: *YFP*: forward-5'-TGCAGTGCTTCGCCCGCTACC-3' and reverse-5'-CCGTCGCCGATGGGGGTGTTC-3' (Mihailovich et al., 2015); *Cre*: forward-5'-GCCTGCATTACCGGTCGATGCAACGA-3' and reverse-5'-GTGGCAGATGGCGCGGCAAACCATT-3' (Basch et al., 2011); *Kmt2a* forward-5'-GAGGTAAGGAGAGTTTTTGCT-3' and reverse-5'-GGTAACACCTTAAAATGCCCT-3' (Kranz et al., 2010); *Kmt2b*: forward-5'-CGGAGGAAGAGAGCAGTGACG-3' and reverse-5'-GGACAGGAGTCACATCTGCTAGG-3' (Glaser et al., 2006).

Assessment of exon 2 deletion of both *Kmt2a* and *Kmt2b*

To determine the entity of *Kmt2* exon 2 deletion, TaqMan assays were performed extracting DNA, through DNeasy Blood and Tissue kit (Qiagen), the day MEFs were plated for transdifferentiation. In particular, Real Time PCR was performed on 7900HT Fast Real-Time PCR system (Applied Biosystems). Primers were the following:

MLL2EX2: forward-5'-GGTCCCCTAAATCAGGAGTTTCAG-3', reverse-5'-GACCG AAGCGCAGAGC-3', reporter sequence-5'-AAGATGTGGCCCCCAGTTC-3'.

MLL1EX2: forward-5'-GCAGTTCTTAGGTTTTGGCTCAGA-3', reverse-5'-GCTTTAT TGGCCATACCTGAAGGA-3', reporter sequence-5'-CTTCGCACTCTGACTTCTTCA -3'.

Western blot for KMT2B

Proteins were extracted in RIPA buffer (10 mM Tris-HCl pH 8, 1% Triton X-100, 0.1% SDS, 0.1% Sodium Deoxycholate, 140 mM NaCl, 1 mM EDTA plus the protease inhibitor cocktail (PIC) (Sigma Aldrich) and Phenylmethanesulfonyl fluoride (PMSF) (0.5 mM) (Sigma Aldrich) from at least 8 x 10^6 MEFs, the day were plated for transdifferentiation.

At least 70 µg of protein extract was loaded into the NuPAGE Novex 3-8% Tris-Acetate Proteins Gels (ThermoFisher Scientific) and run in the NuPAGE Tris-Acetate SDS Running buffer (20X) (ThermoFisher Scientific). Wet transfer was performed at 4 °C, 30V with the Immobilon-P, 0.45 µm, PVDF membrane (Merck Millipore) overnight. Antibodies used are listed in Table S7.

Vector production

BAM and rtTA vectors were generated through calcium phosphate transfection of human embryonic kidney 293T (HEK293T) cells and ultracentrifugation. The following transfer plasmids, deposited by the Wernig Lab in Addgene, were used (Tet-O-FUW-Brn2, Tet-O-FUW-Ascl1, Tet-O-FUW-Myt1l and UbC-rtTA). BAM vectors were produced using a third generation system (envelope plasmid: pMD2-VSV-G; packaging plasmids: pMDLg/pRRE and pRSV-REV).

Image acquisition and analysis: efficiency and cell mortality calculation

Cells were fixed with 4% paraformaldehyde (PFA), 20 minutes on ice and permeabilized with PBS, 10% FBS, 0.1% Triton X-100, 30 minutes at room temperature (RT). Cells were incubated with primary antibodies (listed in Table S7), overnight at 4°C, and then with secondary antibodies 1 h at RT. Primary and secondary antibodies were diluted in PBS, 10% FBS. DAPI (SIGMA D9542) was added to the secondary antibodies mix. A grid of 100 images per embryo in duplicate was acquired. Through ScanR we covered an area of ~ 14 mm^2 per cell density, in a grid of 100 images equidistant from each other, maintaining the same setting across conditions and time points and we acquired at least 1000 cells at day 3 and 500 cells at the following time point. 3 days after plating the number of cells per image was manually evaluated as number of DAPI in each cell density condition. At 13 days only conditions that at day 3 were in the same number were compared. Cells positive for Tuj1 were classified as iNs and manually quantified.

The number of DAPI at day 3 and day 13, of the chosen cell density, were summed and called DAPI start and DAPI end, respectively. To calculate cell mortality the ratio between DAPI start and DAPI end was calculated, assuming that the cells distribute almost equally in the two duplicate wells (*i.e.,* day 3 and day 13) of each condition. Then, to calculate efficiency, the number of $Tuj1^+$ cells at day 13 was related to the number of DAPI start:

$$\frac{number\ of\ Tuj1^{+}_{day13}}{number\ of\ DAPI_{day3}}\%$$

NeuriteTracer was used to calculate neurite length (Pool et al., 2008). Because this calculation depends on the number of neurons the plugin-retrieved value was divided for the number of $Tuj1^+$ cells. Unpaired t test was performed as statistical analysis.

Cytofluorimetric analysis: efficiency and cell mortality calculation

Before cytofluorimentric analysis cells were counted through the Automated Cell Countess (Thermo Fisher Scientific) 5, 7, 9, 13 and 21 days after they were plated

for transdifferentiation. Cell mortality was reported as the percentage of dead cells with respect to the number of plated cells:

$$\frac{N\ of\ plated\ cells - N\ of\ alive\ cells_{day13}}{N\ of\ plated\ cells}\%$$

Knowing the percentage of PSA-NCAM$^+$ cells and the absolute number of cells at day 13, the absolute number of PSA-NCAM$^+$ iNs was calculated. This value was related to the number of plated cells to calculate the efficiency of transdifferentiation:

$$\frac{number\ of\ PSA - NCAM^+_{day13}}{number\ of\ plated\ cells_{day0}}\%$$

FACS sorting

FACS sorting was executed on 4-OHT treated MEFs left in culture 7 days before transdifferentiation. 10^7 MEFs were plated on matrigel coated dishes both for the RNA-seq and the ChIP-seq on iNs at 13 days. Cells were sorted for PSA-NCAM positivity at MoFlo Astrios (Beckman Coulter) with the Software Summit v6.2.

RNA-seq analysis

RNA-seq reads were aligned with TopHat v2.0.10 (Trapnell et al., 2012), first to mm10 Refseq transcriptome, and genes without a perfect alignment were realigned to genome (*--read-realign-edit-dist=1*), tolerating an edit distance of 3. Quantification was performed on the Refseq transcriptome using Cuffquant v2.2.1, with multi-read correction (-u) (Trapnell et al., 2012). This pipeline was selected because it was one of the highest-performing quantification methods in our recent benchmark (Germain et al., 2016).

For the differential expression analysis, we first excluded genes which had an average read count across samples below 50. We used edgeR v.3.12.1 (which outperformed other methods according to our benchmark) with TMM normalization and the exact test on the estimated fragment counts. We considered differentially expressed with high confidence genes with a FDR below 0.01 and an absolute

log2(foldchange) greater than log2(1.5). Differential exon usage analysis was performed with DEXSeq.

Gene Ontology enrichment analyses

Gene Ontology enrichment analyses were performed using the goseq v.1.22.0 R package for RNAseq results in order to correct for RNA-seq transcript length bias (Young et al., 2010), or with the topGO package for ChIPseq results, in both cases using Fisher's test and excluding genes without annotation. Categories with at least 10 genes and maximum 1500 genes were considered. When the number of enriched categories was large, we focused on the most specific categories by removing any category with enriched children categories. Quilts were generated using treemap R package.

RNA-seq validation

The RNA was retrotranscribed through the SuperScript VILO cDNA Synthesis Kit (Invitrogen, 11754-050).

Real Time Quantitative PCR (RT-qPCR) was performed on 7500 Fast Real-Time PCR system (Applied Biosystems) using Sybr green (Applied Biosystems) as detecting reagent and the standard amplification protocol. Primers used are reported in Table S8. Primers for *Magohb* are described in the paper of Ladopoulus et al (Ladopoulos et al., 2013), while the ones for *Syp* in (Simon et al., 2016).

ChIP-seq

At the desired time point, cells were fixed with PBS 1% formaldehyde. Fixation was quenched with 0,125M glycine. Cells were collected in SDS Buffer (100mM NaCl, 50mM Tris-HCl pH 8.1, 5mM EDTA pH 8, 0.5% SDS), centrifuged, then resuspended in 3 ml of ice-cold IP buffer (2 volumes SDS Buffer: 1 volume Triton Dilution Buffer) (Triton Dilution Buffer: 100mM NaCl, 100mM Tris-HCl pH 8.6, 5mM EDTA pH 8, 5%

Triton X-100) and sonicated through the Digital Sonifier 450 (Branson) (ChIP-seq for Menin: 700-bp DNA fragments; ChIP-seq for H3K4me3 and H3K27me3: 200-bp DNA fragments). Immunoprecipitation was performed in IP buffer using the antibodies listed in Table S7.

The immunoprecipitated product was purified through Protein G dynabeads (ThermoFisher Scientific, 10003D), afterwards washed with low-salt (150mM NaCl, 20mM Tris-HCl pH 8, 2mM EDTA pH 8, SDS 0.1%, 1% Triton X-100) and high-salt wash (500mM NaCl, 20mM Tris-HCl pH 8, 2mM EDTA pH 8, SDS 0.1%, 1% Triton X-100) buffer 3 times with 1 ml of 150 mM Wash Buffer and once with 1 ml of 500 mM Wash Buffer with the use of a Dynamag magnet (ThermoFisher Scientific, catalog number 12321D).

Decrossilinking occurred through the incubation of beads (and the 1% input) with Decrosslinking Buffer (1% SDS, 0.1M $NaHCO_3$) at 65 °C overnight. DNA was purified with the QiaQuick PCR Purification kit (Qiagen) following manufacturer's instructions. Libraries were prepared as previously described (Adamo et al., 2015) and sequenced on a HiSeq 2000 instrument (Illumina) following manufacturer's protocol. Sequencing was performed in single end, 50 bp, with a coverage of 30 millions of reads for inputs, H3K4me1 and menin ChIP-seq and 60 millions for H3K27me3.

ChIP-seq reads were trimmed for potential adapter contamination using scythe 0.981 (min 4 nucleotides) before being aligned to the mm10 genome using bowtie 1.0 (Langmead et al., 2009) with –v 2 –m 1, and peaks were called using MACS 2.0.9 (Langmead et al., 2009; Zhang et al., 2008) with default settings. Although we relied mostly on quantitative analyses (below) to compare across replicates and conditions, when comparing peaks directly we considered peaks as overlapping if they shared at least one nucleotide.

Proximally bound genes were defined as having a peak within a -2.5kb/+1kb window around any of their RefSeq TSS. To identify the putative targets of intergenic sites bound by MENIN but in contact with a TSS only through chromatin conformation, we

relied on Hi-C data from the most similar cell type available, namely neural progenitors. We downloaded already processed, statistically significant interactions from the Gene Expression Omnibus entry GSE68582, extracted a bed file containing each region interacting with a RefSeq TSS, and intersected it (using intersectBed) with our regions of interest to find distal targets.

Peak calling is very sensitive to coverage and technical variation, and quantitative analysis of read distribution yields considerably more robust findings. To find differences across conditions, we therefore worked on the distribution of reads falling within relevant genomic windows. For each protein/mark, the windows were defined by merging the enriched regions across samples (*i.e.,* with BedTools: cat *.bed | sortBed -i - | mergeBed -i -). In this way, all regions enriched in at least one sample were considered for statistical testing, without duplicate genomic regions. The read counts were then compared across conditions with edgeR v.3.12.1 (Robinson et al., 2010), using the total number of mapped reads as library size and the TMM method for normalization. Differentially enriched regions were identified using the classical dispersion model of edgeR (based on a negative binomial model) and the exact test.

For the MENIN ChIP-seq, given the low quality of the peak calling (very low and variable number of peaks across samples, probably owing to a low and highly variable coverage), we performed a peak-call-agnostic differential enrichment analysis using diffReps (Shen et al., 2013), which uses sliding windows to directly identify regions of significant difference between sets of enrichment profiles.

Data representation (RNA-seq and ChIP-seq)

Principal component analyses were performed on the normalized, log-transformed read counts (+1 was added before log-transform to avoid errors on null values). Unless specified otherwise, all heatmaps show row z-scores of log-transformed normalized counts. Heatmaps were produced using the pheatmap R package.

External data (RNA-seq and ChIP-seq)

For external datasets, we used the authors' original peak calls (ChIP-seq) or quantification (RNA-seq) that are available from the respective GEO entries.

Exome analysis

The list of Kmt2b dependent genes was predicted by the intersection between DEGs (at FDR < 0.05) and genes with H3K4me3 reduction in *Kmt2b* cKO transdifferentiating MEFs with respect to controls. To test the hypothesis that the coding regions of *KMT2B*-sensitive genes are an untapped reservoir of dystonia-causing mutations, we queried a large repository of whole-exome sequencing (WES) data from a European-descent dystonia cohort. Accrued from movement disorders centers in Munich (Germany), Innsbruck (Austria), and Prague (Czech Republic), this cohort comprised 225 unrelated probands with various types of dystonic presentations in whom disease had not been explained. The recruitment strategy and clinical characterization process have been described previously (Zech et al., 2017) and demographics as well as phenotypic information of the cohort can be found in Table S5. The cohort was enriched for possible Mendelian disease causation, with 48% of probands having an early dystonia onset, 39% having a positive family history for dystonia, and 18% having a generalized distribution of dystonic symptoms. Dystonia was the sole presenting feature in 88% of the probands, whereas the remainder demonstrated additional movement disorders and/or other neurological/extra-neurological signs.

WES of all 225 dystonia subjects had been performed to an average on-target depth of 154x at the Helmholtz Center in Munich (Germany), through enrichment capture using the SureSelect All Exon system (Agilent Technologies) and subsequent paired-end 100-bp sequencing on HiSeq2000/2500 instruments (Illumina) in an automated manner, as described previously (Zech et al., 2017; Zech et al., 2016). For WES summary statistics, see Table S6. Standard protocols for sequence alignment,

variant annotation, genotype quality control, and variant visual inspection had been applied as detailed elsewhere (Zech et al., 2017; Zech et al., 2016). In the dominant model, variants were retained if they were (1) not referenced in the Exome Aggregation Consortium (ExAC) Browser (Lek et al., 2016) and an in-house control exome database (allowing the interrogation of altogether >141,000 control alleles), and (2) predicted to exert a loss-of-function effect (stop-gain/lost, frameshift, and splice-site alterations) or missense/in-frame indel alterations predicted to be among the 1% most deleterious aberrations in the human genome (Combined Annotation Dependent Depletion [CADD] score ≥20) (Kircher et al., 2014) (Figure S6A). In the recessive model, variants were retained if they were (1) present with a minor allele frequency <0.001 in the ExAC Browser and our in-house control exome database, and (2) predicted to exert a loss-of-function effect or missense/in-frame indel alterations predicted to be among the 10% most deleterious aberrations in the human genome (CADD score ≥10)(Kircher et al., 2014) (Figure S6A). As an additional supportive method for selecting the best possible candidate variants and genes, we obtained gene constraint metrics (probability of being loss-of-function intolerant (pLI) and missense Z scores) from the Exome Aggregation Consortium (ExAC) dataset (Lek et al., 2016) for all 216 *KMT2B*-target genes. ExAC-derived pLI scores ≥0.9 indicate that respective genes are intolerant to loss-of-function variation and likely relevant to haploinsufficient disease (Lek et al., 2016) ExAC-derived missense Z scores ≥2.0 indicate that respective genes are depleted of missense variants as compared with mutational expectation and thus more sensitive to this class of variation (Lek et al., 2016).

The top-scoring candidate variants selected from the dominant and recessive models (in the *KMT2B*-target genes *NOL4*, *SLC35F1* and *SLC40A1*) were verified by PCR amplification and conventional Sanger-sequencing.

References

Adamo, A., Atashpaz, S., Germain, P.L., Zanella, M., D'Agostino, G., Albertin, V., Chenoweth, J., Micale, L., Fusco, C., Unger, C.*, et al.* (2015). 7q11.23 dosage-dependent dysregulation in human pluripotent stem cells affects transcriptional programs in disease-relevant lineages. Nature genetics *47*, 132-141.

Basch, M.L., Ohyama, T., Segil, N., and Groves, A.K. (2011). Canonical Notch signaling is not necessary for prosensory induction in the mouse cochlea: insights from a conditional mutant of RBPjkappa. The Journal of neuroscience : the official journal of the Society for Neuroscience *31*, 8046-8058.

Germain, P.L., Vitriolo, A., Adamo, A., Laise, P., Das, V., and Testa, G. (2016). RNAontheBENCH: computational and empirical resources for benchmarking RNAseq quantification and differential expression methods. Nucleic acids research *44*, 5054-5067.

Glaser, S., Schaft, J., Lubitz, S., Vintersten, K., van der Hoeven, F., Tufteland, K.R., Aasland, R., Anastassiadis, K., Ang, S.L., and Stewart, A.F. (2006). Multiple epigenetic maintenance factors implicated by the loss of Mll2 in mouse development. Development *133*, 1423-1432.

Kircher, M., Witten, D.M., Jain, P., O'Roak, B.J., Cooper, G.M., and Shendure, J. (2014). A general framework for estimating the relative pathogenicity of human genetic variants. Nature genetics *46*, 310-315.

Kranz, A., Fu, J., Duerschke, K., Weidlich, S., Naumann, R., Stewart, A.F., and Anastassiadis, K. (2010). An improved Flp deleter mouse in C57Bl/6 based on Flpo recombinase. Genesis *48*, 512-520.

Ladopoulos, V., Hofemeister, H., Hoogenkamp, M., Riggs, A.D., Stewart, A.F., and Bonifer, C. (2013). The histone methyltransferase KMT2B is required for RNA polymerase II association and protection from DNA methylation at the MagohB CpG island promoter. Molecular and cellular biology *33*, 1383-1393.

Langmead, B., Trapnell, C., Pop, M., and Salzberg, S.L. (2009). Ultrafast and memory-efficient alignment of short DNA sequences to the human genome. Genome biology *10*, R25.

Lek, M., Karczewski, K.J., Minikel, E.V., Samocha, K.E., Banks, E., Fennell, T., O'Donnell-Luria, A.H., Ware, J.S., Hill, A.J., Cummings, B.B.*, et al.* (2016). Analysis of protein-coding genetic variation in 60,706 humans. Nature *536*, 285-291.

Mihailovich, M., Bremang, M., Spadotto, V., Musiani, D., Vitale, E., Varano, G., Zambelli, F., Mancuso, F.M., Cairns, D.A., Pavesi, G.*, et al.* (2015). miR-17-92 fine-tunes MYC expression and function to ensure optimal B cell lymphoma growth. Nature communications *6*, 8725.

Pool, M., Thiemann, J., Bar-Or, A., and Fournier, A.E. (2008). NeuriteTracer: a novel ImageJ plugin for automated quantification of neurite outgrowth. Journal of neuroscience methods *168*, 134-139.

Robinson, M.D., McCarthy, D.J., and Smyth, G.K. (2010). edgeR: a Bioconductor package for differential expression analysis of digital gene expression data. Bioinformatics *26*, 139-140.

Shen, L., Shao, N.Y., Liu, X., Maze, I., Feng, J., and Nestler, E.J. (2013). diffReps: detecting differential chromatin modification sites from ChIP-seq data with biological replicates. PloS one *8*, e65598.

Simon, C.M., Janas, A.M., Lotti, F., Tapia, J.C., Pellizzoni, L., and Mentis, G.Z. (2016). A Stem Cell Model of the Motor Circuit Uncouples Motor Neuron Death from Hyperexcitability Induced by SMN Deficiency. Cell reports *16*, 1416-1430.

Trapnell, C., Roberts, A., Goff, L., Pertea, G., Kim, D., Kelley, D.R., Pimentel, H., Salzberg, S.L., Rinn, J.L., and Pachter, L. (2012). Differential gene and transcript expression analysis of RNA-seq experiments with TopHat and Cufflinks. Nature protocols *7*, 562-578.

Vierbuchen, T., Ostermeier, A., Pang, Z.P., Kokubu, Y., Sudhof, T.C., and Wernig, M. (2010). Direct conversion of fibroblasts to functional neurons by defined factors. Nature *463*, 1035-1041.

Young, M.D., Wakefield, M.J., Smyth, G.K., and Oshlack, A. (2010). Gene ontology analysis for RNA-seq: accounting for selection bias. Genome biology *11*, R14.

Zech, M., Boesch, S., Jochim, A., Weber, S., Meindl, T., Schormair, B., Wieland, T., Lunetta, C., Sansone, V., Messner, M.*, et al.* (2017). Clinical exome sequencing in early-onset generalized dystonia and large-scale resequencing follow-up. Movement disorders : official journal of the Movement Disorder Society *32*, 549-559.

Zech, M., Boesch, S., Maier, E.M., Borggraefe, I., Vill, K., Laccone, F., Pilshofer, V., Ceballos-Baumann, A., Alhaddad, B., Berutti, R.*, et al.* (2016). Haploinsufficiency of KMT2B, Encoding the Lysine-Specific Histone Methyltransferase 2B, Results in Early-Onset Generalized Dystonia. American journal of human genetics *99*, 1377-1387.

Zhang, Y., Liu, T., Meyer, C.A., Eeckhoute, J., Johnson, D.S., Bernstein, B.E., Nusbaum, C., Myers, R.M., Brown, M., Li, W.*, et al.* (2008). Model-based analysis of ChIP-Seq (MACS). Genome biology *9*, R137.